

A comparison of moderate and high spatial resolution satellite data for modeling gross primary production and transpiration of native prairie, alfalfa, and winter wheat

Jorge Celis^a, Xiangming Xiao^{a,*}, Pradeep Wagle^b, Jeffrey Basara^c, Heather McCarthy^a, Lara Souza^a

^a Department of Microbiology and Plant Biology, Center for Earth Observation and Modeling, University of Oklahoma, Norman, OK 73019, USA

^b USDA-Agricultural Research Service, Oklahoma and Central Plains Agricultural Research Center, El Reno, OK 73360, USA

^c Department of Environmental, Earth, and Atmospheric Sciences at University of Massachusetts Lowell, MA, USA

ARTICLE INFO

Keywords:

Vegetation photosynthesis model
Vegetation transpiration model
CO₂
Water use
Remote sensing
Precision farming

ABSTRACT

Although agroecosystems have a significant potential to offset carbon dioxide (CO₂), the amount of CO₂ captured can vary significantly depending on management practices. Accurate estimation of gross primary production (GPP) and transpiration (T) of agroecosystems at the field scale are essential for the study of food security and water resource management. To date, the carbon and water fluxes data products for commercial agroecosystems are limited, mostly at the moderate spatial resolution (MSR, hundreds of meters), which cannot be used to assess the temporal dynamics of GPP and T at the field scale. This study used the vegetation photosynthesis model (VPM) and vegetation transpiration model (VTM) to estimate field-level daily GPP (GPP_{VPM}) and T (T_{VTM}), respectively, in native prairie, alfalfa (*Medicago sativa* L.), and winter wheat (*Triticum aestivum* L.) in central Oklahoma, USA. We evaluated the reliability and advantages of vegetation indices (enhanced vegetation index, EVI and land surface water index, LSWI) in monitoring the land surface phenology using moderate spatial resolution data from Moderate Resolution Imaging Spectroradiometer (MODIS) and high spatial resolution (HSR, tens of meters) data from Landsat and Sentinel-2. The accuracy of GPP_{VPM} and T_{VTM} estimates at different spatial scales was evaluated using GPP (GPP_{EC}) and evapotranspiration (ET_{EC}) from the eddy flux tower sites, respectively. Results demonstrate the capacity of VPM and VTM to estimate the field-level carbon and water flux dynamics and their responses to weather conditions. The use of HSR vegetation indices helped to address certain challenges faced by MSR indices, especially in capturing the crop phenology in smaller areas with conservation measures or disturbances. The findings highlight the importance of using HSR GPP estimates to reduce uncertainty in quantifying CO₂ fluxes for croplands and grasslands. The findings also demonstrate the ability of the models to track field-level vegetation phenology, carbon uptake, and water use in agroecosystems under different management practices.

1. Introduction

Monitoring crop productivity and improving water use of croplands and grasslands is essential for food security and sustainable agriculture, particularly with the growing food demand and the increasing challenges in the supply chain, land availability, and field productivity (Barrett, 2021; Tilman et al., 2011). Native prairie is important for livestock production and has been extensively transformed into pastures (e.g., alfalfa, *Medicago sativa* L.) and croplands (e.g., winter wheat, *Triticum aestivum* L.) in the U.S. Southern Great Plains (Bajgain et al., 2018).

Alfalfa is a high-quality perennial legume used for cattle grazing or hay harvest (Wagle et al., 2019a). Winter wheat is one of the most widely grown grain crops in the world and is often used for dual-purpose (cattle grazing and grain production) in the U.S. Southern Great Plains (Redmon et al., 1995; Wagle et al., 2018). Grasslands and croplands have varying potentials for carbon sequestration, dependent upon climate and different management practices (Guan et al., 2016). As the gross primary production (GPP) of native tallgrass prairie, alfalfa, and winter wheat is affected substantially by varying climates and management practices, it is important to better model and predict their responses to variable climates (Hlisenkovský et al., 2023; Tucker et al., 1971).

* Corresponding author at: University of Oklahoma
E-mail address: xiangming.xiao@ou.edu (X. Xiao).

Nomenclatures*Acronyms and Abbreviations*

APAR	Absorbed photosynthetically active radiation	MODIS	Moderate Resolution Imaging Spectroradiometer
APAR _{chl}	Absorbed photosynthetically active radiation by the chlorophyll	MSR	Moderate spatial resolution
CO ₂	Carbon dioxide	NBP	Net ecosystem carbon balance
c _p	Specific heat	NDVI	Normalized differentiate vegetation index
E	Evaporation	NEE	Net ecosystem exchange
E _{bs}	Bare soil evaporation	NPP	Net primary production
EC	Eddy covariance	NPV	Non-photosynthetically active vegetation
ECOSTRESS	The Ecosystem Spaceborne Thermal Radiometer Experiment on Space Station	P-M	Penman-Monteit
ECT	Eddy covariance tower	PAR	Photosynthetically active radiation
ER	Ecosystem respiration	PAV	Photosynthetically active vegetation (chloroplast)
ET	Evapotranspiration	PPFD	Photosynthetic photon flux density
ET _{EC}	Evapotranspiration derived from the ECT	QC	Quality controls
EVI	Enhanced vegetation index	r _a	Aerodynamic resistance
fPAR	Fraction of photosynthetically active radiation	r _c	Canopy stomatal resistance
G	Ground soil heat flux	Rn	Net radiation
GPP	Gross primary production.	SEB	Surface energy balance
GPP _{EC}	Gross primary production estimates from the ECT.	SW	Total incoming shortwave solar radiation
GPP _{VPM-MOD}	Gross primary production estimates from VTM at MSR.	SWIR	Shortwave infrared
GPP _{VPM-LS2}	Gross primary production estimates from the VTM at HSR.	T	Transpiration
H	Sensible heat flux	T _{VTM-EC}	Transpiration estimates from VTM using EC data as input
HSR	High spatial resolution	T _{VTM-MOD}	Transpiration estimates from VTM using MSR data as input
IR	Infrared	T _{VTM-LS2}	Transpiration estimates from VTM using HSR data as input
LE	Latent heat flux	TIR	Thermal infrared
LST	Land surface temperature	T _{opt}	Optimal air temperature for photosynthesis
LSWI	Land surface water index	u*	friction velocity
LUE(ε _g)	Light use efficiency	Vis	Vegetation indices
LUE0(ε ₀)	Maximum light use efficiency	VPD	Vapor pressure deficit
		VPM	Vegetation photosynthesis model
		VTM	Vegetation transpiration model
		WUE	Water use efficiency
		γ	Psychrometric constant
		Δ	Vapor pressure–air temperature curve
		ρ	Air density

Vegetation indices (VIs – which indicates different aspects of vegetation) from optical sensors (e.g., Moderate Resolution Imaging Spectroradiometer MODIS) have been used to support crop monitoring and delineate spatio-temporal variability of crop development (Duchemin et al., 2006). However, operational monitoring of crop phenology in feedstock systems is a challenging task due to field sizes and shape, different planting patterns, multiple crops and rotations, and the lack of consistent continuous observations at high spatial resolutions (Dong et al., 2020; Huang et al., 2019b; Misra et al., 2020; Peña-Barragán et al., 2011).

Gross primary production is the largest carbon flux in terrestrial ecosystems, and it represents the CO₂ captured by vegetation via photosynthesis (Beer et al., 2010; Campbell et al., 2017). GPP is crucial for the ecosystem's biomass production (Lambers et al., 2008), and it is often used as one of the major variables in assessing the terrestrial carbon cycle and crop productivity. Since GPP cannot be directly measured at the ecosystem scale, there are many techniques to model and predict it, including machine learning algorithms based on eddy covariance (EC) data, process-based models, statistical models, and light use efficiency (LUE) models (Celis et al., 2023; Joiner et al., 2018; Mäkelä et al., 2008; Wu et al., 2010; Yuan et al., 2007). The LUE-based GPP models are widely used due to simplicity and data availability (Celis et al., 2023; Zhang et al., 2017). The LUE-based GPP models are based on solar energy that is absorbed by vegetation (light absorption) and LUE that is affected by environmental conditions (e.g., temperature and water stress) (Chang et al., 2021; M. M. Huang et al., 2019). The LUE-based GPP models can be categorized based on their approaches for computing (1) the amount of light absorption and (2) the LUE. Some

LUE models estimate light absorption by vegetation canopy (APAR_{canopy}) (Jacquemoud et al., 2009; Running et al., 2015), while some LUE models estimate light absorption by chlorophyll in the canopy (APAR_{chl}) (Wang and Leuning, 1998; Xiao et al., 2004). Zhang et al. (2017) highlighted the limitation and impact of the APAR_{canopy} in the LUE-based MOD17 GPP product (Running et al., 2004) to represent the seasonal changes in vegetation photosynthetic capacity, resulting in moderate to large underestimation of GPP in croplands and grasslands (Wagle et al., 2014) as shown in cross-site synthesis studies (Wang et al., 2017). Studies have underlined the strong performance of the vegetation photosynthesis model (VPM), which uses the energy absorbed by chlorophyll (APAR_{chl}) to estimate daily GPP (Xiao et al., 2004; Zhang et al., 2017). Secondly, there are different ways to estimate maximum LUE and assess the effects of environmental factors (e.g., air temperature and water stress) on LUE (Chang et al., 2020; Zheng et al., 2018). However, many LUE-GPP models presume one optimum air temperature (T^{opt-biome}) for individual biome types under variable climates. The T^{opt} varies over time and across sites (Wagle et al., 2015a), and the assumption of a constant T^{opt-biome} for individual biomes can lead to significant uncertainties in GPP estimates (Richardson et al., 2012). In fact, a recent study by Chang et al. (2021) shows that these uncertainties could be as high as 10 Pg C/yr on the global scale. Other studies have also highlighted the importance of accounting for the effects of changing air temperatures on photosynthesis and GPP, particularly in the context of changing climate (Huang et al., 2019b; Xu et al., 2013). These studies underscore the need for improved models that can effectively capture the complex relationships among photosynthesis, temperature, and other environmental factors.

Transpiration (T), the largest component of evapotranspiration (ET) in agroecosystems, is essential for crop growth assessment (Celis et al., 2023). Measured T data products at the field scale are not available and often derived from partitioning ET [ET = evaporation (E – unproductive water loss) + T (productive water loss)]. Accurate T estimates are helpful to reduce E losses, improve irrigation scheduling, reduce costs of water and energy, and consequently support food security and improve water use efficiency (i.e., gain of carbon/water use) under the premise of growing more food with less water (Li et al., 2018; Liliane and Charles, 2020; Wang et al., 2020). Nonetheless, the use of T and ET in agroecosystems at the field level is limited due to the spatial resolution of existing remote sensing data products (Ai et al., 2020; Allen et al., 2007; Zhang et al., 2016), the inability to directly measure T at the field scale, the cost of deploying instrumentation to estimate T and ET over multiple fields in a single farm operation, and the complexity and uncertainty of ET partitioning methods (Kool et al., 2014). The Penman-Monteith (PM) approach (Monteith, 1965; Penman, 1948) has been successfully incorporated into multiple physical-based hydrological (Ivanov et al., 2004) and agro-hydrological models with high accuracy in their T and ET estimates (Celis, 2019). However, the use and transferability of these models are limited, given their extensive parametrizations and dependence on multiple physical variables that are not readily available. In addition, these models and other approaches using the PM equation have lower reliability in agroecosystems, due to structural uncertainties introduced by using static biophysical parameters (Mahfouf et al., 1996; Matsui et al., 2005; Vivoni et al., 2007).

Satellite ET products such as MOD16 (Mu et al., 2011) are open source and frequently used to estimate ET in agroecosystems, but they have limitations due to factors such as cloud cover, water stress, and the coarse spatial (500 m) and temporal (8-day) resolutions of the data. Multiple studies have reported poor accuracy of the MOD16 ET product in multiple agroecosystems, particularly larger biases in irrigated fields (Souza et al., 2019; Velpuri et al., 2013). On the other hand, newer products like ECOSTRESS (Meerdink et al., 2019), which is freely available to the public at higher spatial resolution (70 m) and calculates ET based on land-surface temperature, have limitations as well. The limitations include infrequent revisit times, lack of ground-based validation, and structural uncertainties like a 0.85 °C cold bias in retrievals from temperatures below 21.85 °C (Hulley et al., 2022). Furthermore, several studies have reported overestimations of the ECOSTRESS (ECO3ETPTJPL and ECO3TEALEXI) data products in different landcover types including temperate humid forest (Liu et al., 2021), crop and grasslands ecosystems with significant positive bias in the instantaneous ET data product during morning time when compared with in-situ ET EC data ($R^2 = 0.23$), and moderate linear relationships of the daily ET products ($R^2 = 0.40$ and RMSE >40 W/m²) in agricultural landcover (Liang et al., 2022). The poor ET estimates directly impact the reliability and potential use for field-level water management and crop yield predictions. For these reasons, there is a need for a simpler, more accurate, and more transferable technique to obtain accurate T estimates at the field level in croplands and grasslands.

This study employed VPM to estimate GPP and vegetation transpiration model (VTM) (Alfieri et al., 2009) to estimate T in native prairie, alfalfa, and winter wheat flux sites in Oklahoma, USA. The major objectives of this study include: (1) assessing the consistency of vegetation indices (enhanced vegetation index, EVI and land surface water index, LSWI) from moderate spatial resolution (MSR - MODIS) and high spatial resolution (HSR - Landsat and Sentinel-2) images in tracking the land surface phenology and physiology of native prairie, alfalfa, and winter wheat, and (2) evaluating the performance of VPM in estimating GPP and VTM in estimating T in native prairie, alfalfa, and winter wheat using MSR and HSR images. This study improves our understanding of how spatial resolution affects the representation of carbon and water dynamics in cropland and grassland ecosystems, and how these dynamics vary in various land use types used for animal feeding. Improving our understanding of the effects of different management

practices on carbon and water dynamics will allow us to make more informed decisions about sustainable agriculture.

2. Materials and methods

2.1. Study sites

In this study, we selected three sites with different land cover types (native tallgrass prairie, alfalfa, and winter wheat) in central Oklahoma, USA. The sites are located at the USDA-ARS, Oklahoma and Central Plains Agricultural Research Center, El Reno, Oklahoma. The study area, displayed in Fig. 1, has a temperate continental climate, with an average (1981–2010) annual air temperature of 15 °C and mean annual precipitation of 925 mm (Wagle et al., 2019a).

The tallgrass prairie site (35.5419 N, 98.0195°W), covering 32 ha, was divided into nine paddocks. Eight paddocks were used for livestock grazing and one paddock was set as a control (no livestock grazing). The eight paddocks were rotationally grazed from 23 to 60-day periods by 11 to 16 heads of yearling stocker cattle from May through July (Wagle et al., 2020). The soils are a diverse range of Mollisol, showcasing distinct families and subgroups with the Norge series silt loams being the most common soil type (Wagle et al., 2019). The dominant species at the site were warm-season grasses such as big bluestem (*Andropogon gerardii* Vitman), indiagrass (*Sorghastrum nutans* (L.) Nash), and little bluestem (*Schizachyrium scoparium* (Michx.) Nash) (Wagle et al., 2020). In this study, we used satellite observations from paddock (P18-R4) with an area of 4.95 ha and a flux tower system as most contribution of eddy fluxes was limited to this paddock (Wagle et al., 2020). This paddock was grazed by 16 cattle heads between June 15 and July 31 in 2016, May 9 and July 8 in 2017, and May 23 and July 8 in 2018. According to previous works (Fischer et al., 2012; Northup et al., 2002), aboveground biomass production by mid-July is between 2 and 3 tons/ha (drought years) and 3–6.5 tons/ha (wet years), and planned level of forage removal by livestock grazing, which can be considered a field disturbance was approximately 1.5 ton/ha per year (Wagle et al., 2020).

The Alfalfa site (35.5752 N, 98.0549°W), covering 48 ha, is located at a low terrace adjacent to the bottomland along a permanent stream. The soil type is Dale (Fine-silty, mixed, thermic, Pachic Haplustolls) series, like silt loam. Alfalfa (cv. Cimarron 400) was planted in Fall 2012. The field was harvested for hay periodically during each growing season to provide forage for dairy cattle (Wagle et al., 2019a). The harvest dates in 2016 were May 18th, June 17th, July 13th, and October 7th. The harvest dates in 2017 were May 3rd, June 7th, July 6th, August 9th, and September 14th. Only the first harvest on May 17th, 2018 was included in our study period.

The winter wheat (cv. Gallagher) site (35.5643°N, 98.0614°W), covering 28 ha, was sown at 19 cm row spacing and managed for high production potential using management practices common to the region, including fertilizer, herbicide, and pesticide applications (Wagle et al., 2018). Soils are a complex of Renfrow-Kirkland silt loams, Bethansilt loams, and Norge silt loams (Mollisols) with an average pH ≤ 5.8 , electrical conductivity $< 300 \mu\text{Scm}^{-1}$, and soil bulk density (ρ_b) of 1.34–1.45 g cm⁻³ (USDA-NRCS, 1999). The winter wheat site (E1 – no-till field) was used for both livestock grazing and grain production during the 2017–2018 growing season, and grain production only during the 2016–2017 and 2019–2020 growing seasons (Wagle et al., 2021).

2.2. Climate and CO₂ flux data from the EC flux tower sites

The EC measurements at the tallgrass prairie site were collected during the 2016 growing season (April–October) and from June 2017 to September 2018. The EC system at the alfalfa site was installed in late March 2016 near the center of the 48 ha field (Wagle et al., 2019). Data were collected for two years until May 2018. For the winter wheat site, the EC system was installed near the center of the field in September

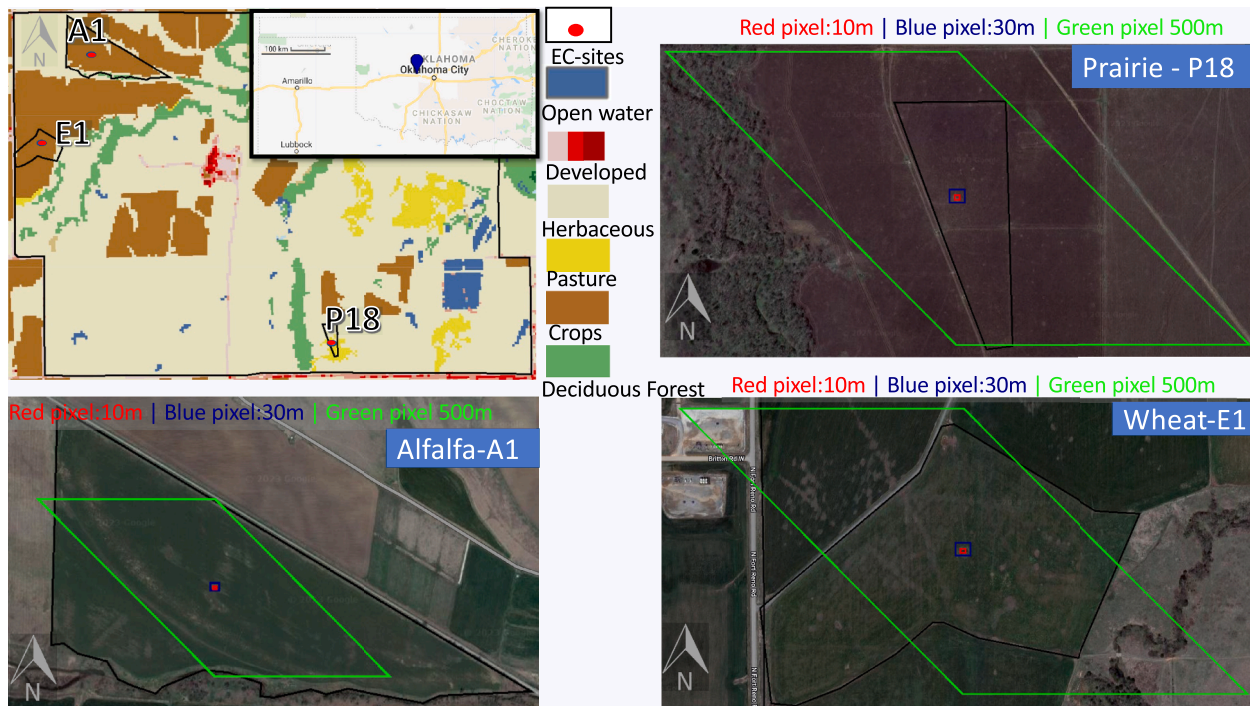


Fig. 1. The geographical locations and landscapes of the three study sites. The top left displays the study sites' landcover map from the NLCD 2016. The longitude and latitude position information of the three eddy covariance (EC) flux tower sites (red dot). The individual fields P18, A1, and E1 are centered at the EC location with field boundaries in black with one 10 m Sentinel-2 pixel (red polygon), 30 m Landsat pixel (blue polygon), and Moderate Resolution Imaging Spectroradiometer (MODIS) pixel at 500 m (green polygon) spatial resolutions.

2016.

The EC systems in the three towers have an open-path infrared gas analyzer (LI-7500 RS, LI-COR Inc., NE, USA) and a 3-D CSAT3 sonic anemometer (Campbell Scientific Inc., UT, USA). The measurement height for all the EC towers in this study is 2.5 m from the ground surface with a fetch >200 m radius in most directions, and the EC data are collected at a 10 Hz frequency. Previous studies in these sites showed that over 80 % of the contribution to EC-measured fluxes was received from <100 m upwind distance of the flux towers (Wagle et al., 2018, 2020). The EddyPro software version 6.2.0 (LI-COR Inc., NE, USA) was used to process raw EC data to obtain 30-min fluxes. Fluxes were screened for bad quality flags, unreliable fluxes, and outliers (greater than 3.5 times of standard deviation based on a 14-day running window) (Wagle et al., 2015b, 2019a, 2019). There are no observation techniques available to measure GPP directly at the field scale (Ma et al., 2015). As a result, GPP can only be inferred from the partitioning of net ecosystem CO₂ exchange (NEE), measured by EC systems based on the covariance between fluctuations in vertical wind velocity and fluctuations in the concentration of CO₂ (Anav et al., 2015; Reichstein et al., 2005). The REdDyProc package from the Max Planck Institute for Biogeochemistry, Germany was used to fill gaps in flux and meteorological data and to partition NEE into GPP and ecosystem respiration (ER) (Wagle et al., 2020). The GPP was calculated as the difference between the measured NEE and estimated ER that is estimated by the model based on the exponential relationships between air temperature and nighttime NEE (Cabral et al., 2013; Reichstein et al., 2002, 2005). The latent heat (LE) flux was used to calculate evapotranspiration (ET). The energy balance closure [EBC = (sensible heat + LE)/(net radiation - soil heat flux)], without any correction terms, for these sites was around 0.75–80 % (Bajgain et al., 2018; Wagle et al., 2018), typical for the most EC flux sites. More details are available in previous studies (Wagle et al., 2019a, 2019b, 2020). The time series of daily GPP fluxes were averaged at 8-day intervals to match the temporal resolution of the remote sensing-derived vegetation indices.

Climate data for all three sites during 1/2016 - 11/2022 were

obtained from the nearby El Reno Oklahoma Mesonet Station (ELRE, 35.5484°N, 98.0365°W) (McPherson et al., 2007). Hourly air temperature and rainfall data were aggregated into daily averages and daily sums, respectively. Photosynthetically active radiation (PAR) data were estimated as 0.48 of total incoming shortwave radiation and converted into photosynthetic photon flux density (PPFD) using the approximation $1 \text{ W m}^{-2} \approx 4.57 \mu\text{mol m}^{-2} \text{ s}^{-1}$ (Thimijan and Heins, 1983).

2.3. Land surface reflectance and vegetation indices from MODIS, Landsat, and Sentinel-2 images

The MOD09A1 Collection 6 product (Vermote et al., 2015) provides 8-day estimates of surface reflectance at a 500 m spatial resolution. Two vegetation indices (VIs) for the MOD09A1 collection were calculated on Google Earth Engine (GEE) using the surface reflectance data. The quality band (QA), VIs, and surface reflectance time series were downloaded and assessed for quality control and used in the model. The enhanced vegetation index (EVI) (Huete et al., 1997) (Eq. (1)) and land surface water index (LSWI) (Xiao et al., 2004a.) (Eq. (2)) were calculated from surface reflectance data from blue, red, near infrared (NIR), and shortwave infrared (SWIR) bands.

$$\text{EVI} = 2.5 \times (\text{NIR} - \text{Red}) / (\text{NIR} + 6 \times \text{Red} - 7.5 \times \text{Blue} + 1) \quad (1)$$

$$\text{LSWI} = (\text{NIR} - \text{SWIR}) / (\text{NIR} + \text{SWIR}) \quad (2)$$

Landsat provides surface reflectance data at 30 m spatial resolution and 16-day temporal resolution. In this study, we used the atmospherically corrected surface reflectance data from the Landsat 7 ETM+ sensor and the operational land imager (OLI) Landsat 8 OLI/TIRS sensors. The VIs were calculated for all the images available on GEE, and the time series VIs and surface reflectance data over the flux tower sites were downloaded and inspected for quality control using a cloud, shadow, water, and snow mask (Foga et al., 2017). In addition, the blue band was used to detect and remove dates with the presence of any cloudy and water pixels (Du et al., 2002).

Sentinel-2 (S2) is a wide-swath (290 km), high-resolution, multi-spectral imaging with a global 10-day revisit (or 5-day revisit if both S2 satellites are combined). S2-A/B has 13 spectral bands: three for atmospheric correction (60 m), four visible and NIR bands (10 m), and six red-edge, NIR and SWIR bands (20 m), and the VNIR and SWIR bands have similar spectral coverage to Landsat 8 (OLI/TIRS) (Storey et al., 2016). In this study, we used the S2 orthorectified atmospherically corrected surface reflectance from a multispectral Instrument (MSI) available on GEE. The surface reflectance data quality control was completed after downloading the pixel time series, using the cloud bit mask, cirrus bit mask, and the blue band for detecting and removing dates with the presence of cloudy and water pixels (Du et al., 2002).

The combined use of Landsat and Sentinel-2 provides a global average revisit of 4.6 days (Li and Roy, 2017). Furthermore, both systems provide a 12-bit radiometric resolution with similar reflective wavelengths (Drusch et al., 2012; Gascon et al., 2017; Irons et al., 2012) and information sensed over the same areas. The similarities between Landsat and Sentinel-2 spectral resolutions facilitate the combined use of their datasets in several different ways including data fusion, as reported in previous studies. (Zhang et al., 2018). In this study, the surface reflectance time series data from Landsat and Sentinel-2 were combined without resampling the Landsat 30 m data into 10 m data, since the pixel chosen was within the tower footprint (within 100 m radius of the tower) (Wagle et al., 2018), but at least 30 m away from the EC tower to avoid biases due to field-instrument management and disturbances. For the pixel, time series Landsat and Sentinel-2 observations were combined by their acquisition dates, and for those observations with overlapping dates from the two products, one observation was chosen based on the data quality (i.e., maximum NDVI) as in past studies (Gascon et al., 2017; Markham et al., 2014; Zhang et al., 2018). The resulting time series Landsat/Sentinel-2 data were used as input for daily simulations of GPP and T. For comparison with 8-day MODIS composites, the combined time-series of optical data were further aggregated into 8-day composite data for VPM/VTM model simulations.

2.4. Land surface phenology

The land surface phenology (LSP) includes the start of the growing season (SOS), the end of the growing season (EOS), and the growing season length (GSL). The seasonal dynamics of the vegetation indices (EVI and LSWI) at the three sites reveal the LSP metrics in terms of the canopy structure and the process of crop development during the growing season. The EVI is related to chlorophyll content in the canopy and the LSWI is related to the water content in the canopy and soil surface (Xiao et al., 2009). Both EVI and LSWI have been used to identify the SOS and EOS. For example, the VI-based SOS is the starting period of $EVI > 0.1$ and $LSWI > 0$ in the spring, a criterion successfully applied over several types of crops and grasses (Xin et al., 2020; Zhang et al., 2022). The transition from $LSWI < 0$ and $LSWI > 0$ in the spring represents the emergence of green leaves, while the reverse transition from $LSWI > 0$ to $LSWI < 0$ in the fall/winter indicates the change from green plants to senescent phase.

In this study, we used the vegetation indices (VI-based) method to identify the SOS ($EVI > 0.1$ and $LSWI > 0$) and the EOS ($EVI < 0.1$ and $LSWI < 0$). The accuracy of the VI-based method and thresholds used were compared using the EC-derived GPP data, where the SOS is the third continuous data point of $GPP > 1 \text{ g C m}^{-2}$ and the EOS takes place after 3 consecutive time periods of $GPP < 1 \text{ g C m}^{-2}$.

2.5. Vegetation photosynthesis model (VPM)

Eight-day average daily GPP ($\text{g C/m}^2/\text{day}$) is estimated using VPM (Xiao et al., 2004), which calculates the amount of solar energy absorbed by vegetation chlorophyll ($APAR_{chl}$) and the light use efficiency (LUE_g). The EVI is used as a proxy for $FPAR_{chl}$ (5).

$$GPP = APAR_{chl} * LUE_g \quad (3)$$

$$APAR_{chl} = FPAR_{chl} * PAR \quad (4)$$

$$FPAR_{chl} = (EVI - 0.1) * 1.25 \quad (5)$$

$$LUE_g = LUE_0 * T_{scalar} * W_{scalar} \quad (6)$$

LUE_0 is the apparent quantum yield or maximum light use efficiency ($\mu\text{mol CO}_2 / \mu\text{mol PPF}$) and it has different values for C3 and C4 plants in the VPM. The LUE_0 value used for C3 plants in our study was $0.42 \text{ g C mol}^{-1} \text{ PPF}$, while the value for C4 vegetation was $0.64 \text{ g C mol}^{-1} \text{ PPF}$ (Ma et al., 2018; Yuan et al., 2007; Zhang et al., 2017). The VPM accounts for the presence of C3 and C4 plants in those areas that have both C3 and C4 plants by including the fractions of C3 plants (C3F) and C4 plants (C4F). The native tallgrass prairie site in this study is a mix of C3 and C4 vegetation, and the mixing ratio used in the models was 20 % C3F and 80 % C4F considering the presence of cool-season C3 grasses in spring and late fall and the domination of warm-season C4 grasses in summer.

$$LUE_0 = LUE_{0-C3} * C3F + LUE_{0-C4} * C4F \quad (7)$$

The effects of air temperature and water stress on GPP (Chang et al., 2021; M. M. Huang et al., 2019) are introduced by T_{scalar} and W_{scalar} , respectively. The LSWI was used to calculate W_{scalar} (Eq. (8)). The T_{scalar} was computed based on the Terrestrial Ecosystem Model (TEM) (Raich et al., 1991).

$$W_{scalar} = \frac{1 + LSWI}{1 + LSWI_{max}} \quad (8)$$

$$T_{scalar} = \frac{(T^{\circ} - T^{\circ}_{min})(T^{\circ} - T^{\circ}_{max})}{[(T^{\circ} - T^{\circ}_{min})(T^{\circ} - T^{\circ}_{max})] - (T^{\circ} - T^{\circ}_{opt})^2} \quad (9)$$

where T° is the air temperature, and T°_{min} , T°_{opt} , and T°_{max} , are the minimum, optimum, and maximum temperatures for photosynthesis, respectively. The biome-specific T°_{min} , T°_{opt} , and T°_{max} values are 0°C , 27°C , and 48°C for grasslands, and -1°C , 30°C , and 48°C for croplands (Zhang et al., 2017). In this study, we used the same procedure reported in the previous publication (Xin et al., 2020) to estimate site-specific T°_{opt} from the relationship between GPP_{EC} or vegetation index (EVI) and daily daytime mean air temperature (T°_{DT}) (see Results 3.3 for more details).

To determine the effects of satellite images data with different spatial resolutions on GPP estimates, we carried out two sets of VPM simulations to estimate daily GPP by using site climate data and (1) time series EVI and LSWI data from Landsat and Sentinel-2 (GPP_{VPM-LS}) and (2) time series EVI and LSWI data from MODIS ($GPP_{VPM-MOD}$).

2.6. Vegetation transpiration model (VTM)

Evapotranspiration is the combined water flux of evaporation (E) from soil and canopy-intercepted water, and transpiration (T) from plants (Segovia-Cardozo et al., 2022). During the plant growing season, T represents the largest component of ET and is often larger than E (Ben-Asher et al., 2006; Paul-Limoges et al., 2022; Puig-Sirera et al., 2021). At the leaf level, photosynthesis or carbon gain (GPP) and T are closely coupled, and water use efficiency at the leaf level is often calculated as their ratio (i.e., $WUE_{Leaf} = GPP/T$, $\text{mol CO}_2 / \text{mol H}_2\text{O}$). The VTM estimates daily T as a function of GPP and WUE_{Leaf} , and it was evaluated in grasslands (Alfieri et al., 2009). $WUE_{Leaf,C3}$ for C3 plants is $500 \mu\text{mol CO}_2 / \mu\text{mol H}_2\text{O}$ and $WUE_{Leaf,C4}$ for C4 plants is $250 \mu\text{mol CO}_2 / \mu\text{mol H}_2\text{O}$ (Taiz et al., 2015). The equations below take into consideration the presence of different vegetation types within a field, including the fraction of C3 vegetation (C3F) and C4 vegetation (C4F).

$$T = (C3F * 1 / WUE_{Leaf-C3} + C4F * 1 / WUE_{Leaf-C4}) * GPP \quad (11)$$

$$\text{IfC3F} = 1.0, T(\text{mmH}_2\text{O} / \text{day}) = 0.33(\text{mmH}_2\text{O} / \text{gC} / \text{m}^2 / \text{day}) * \text{GPP}(\text{gC} / \text{m}^2 / \text{day}) \text{ for C3 plants} \quad (12)$$

$$\text{IfC4F} = 1.0, T(\text{mmH}_2\text{O} / \text{day}) = 0.165(\text{mmH}_2\text{O} / \text{gC} / \text{m}^2 / \text{day}) * \text{GPP}(\text{gC} / \text{m}^2 / \text{day}) \text{ for C4 plants} \quad (13)$$

2.7. Statistical analysis

We performed simple and multiple linear regression analyses between GPP and vegetation indices derived from MODIS, Landsat, and Sentinel-2 images. For the analyses between MODIS-based VIs and GPP, we used 8-day average GPP data to match their temporal resolutions. For the analyses between GPP and Landsat/Sentinel-2 images, we used 7-day GPP data (3 days before and 3 days after the Landsat/Sentinel-2 image acquisition dates) as in a previous study (Wagle et al., 2020). The metrics to assess those relationships between GPP and satellite-derived VIs were R^2 (the coefficient of determination), the Pearson correlation coefficient (r) to measure the fit of the data to the regression line, the mean absolute error (MAE), and the normalized root means squared error (nRMSE).

3. Results

3.1. Seasonal dynamics of climate, vegetation indices, and carbon fluxes

Photosynthetically active radiation had strong seasonal dynamics, with peaks in the summer and troughs in the winter (Fig. 2). The 8-day average PAR values ranged from 11.5 mol/m²/day to 60.0 mol/m²/day. Air temperature (T_{air}) had strong seasonal dynamics during 2016–2019, characterized by a April to October (July warmest month) and a cold season from November to March (December coldest month in

average) (Figs. 2a, 3a, 4a). The 8-day average T_{air} ranged from $-5.2\text{ }^\circ\text{C}$ in the winter to $30\text{ }^\circ\text{C}$ in the summer. The seasonal distribution of rainfall is characterized by a wet spring, a dry summer, and a wet fall (Figs. 2a, 3a, 4a). April and May usually had the largest monthly rainfall. The annual rainfall was 631 mm (2016), 795 mm (2018), 1084 mm (2019), and 1109 mm (2017).

At the tallgrass prairie site, the vegetation index data (Fig. 2b) showed strong seasonal dynamics. Grasses started to green up in April and became senescent after October. The GPP_{EC} increased at the beginning of spring with a steep rise in April and reached maximum values in May (Fig. 2c). The GPP_{EC} was high in the spring of 2016 and in the fall of 2017 and 2018, which was mainly driven by high rainfall. The EOS started at the beginning of November and GPP values decreased to $\leq 1\text{ g C/m}^2/\text{day}$. VIs derived from both MSR and HSR data displayed consistent seasonality and magnitudes. The combined use of Landsat-Sentinel-2 enables us to generate consistent time series with a temporal resolution comparable with MODIS. For this site, LSWI_{HSR} showed higher sensitivity to field disturbances events like grazing.

At the alfalfa site, the large variations in vegetation indices and CO_2 fluxes (NEE and GPP) (Fig. 3) corresponded to the multiple hay harvest events in a year (e.g., five harvests in 2017). During the 2016–2019 study period, 2017 was the wettest year (1109 mm), and GPP_{EC} was higher in 2017 than in 2016 (Fig. 3c). The ET_{EC} had a relatively smaller magnitude of change than CO_2 fluxes. By late October, GPP_{EC} declined substantially and fell below $1\text{ g C/m}^2/\text{day}$, indicating the EOS of vegetation. EVI derived from Landsat-Sentinel-2 displayed clear patterns and captured well harvest events like the ones reported in 2017. On the other

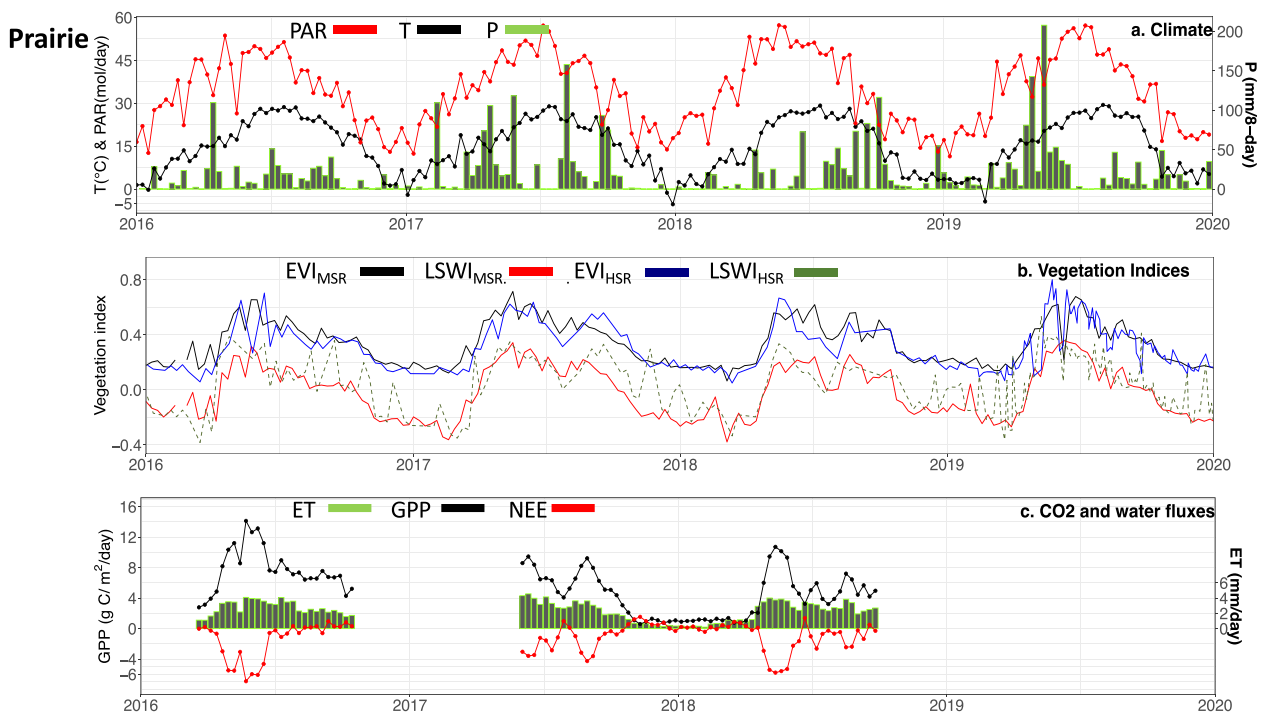


Fig. 2. The seasonal dynamics and interannual variation of climate, vegetation indices, carbon and water fluxes from the prairie site. a.) Air temperature(T), photosynthetically active radiation (PAR), and precipitation. T and PAR are 8-day mean values, and precipitation is 8-day sum values. b.) Vegetation indices (enhanced vegetation index (EVI) and land surface water index (LSWI)) derived from MODIS at the 8-day interval and Landsat-Sentinel2. c.) NEE_{EC} , GPP_{EC} , and ET_{EC} .

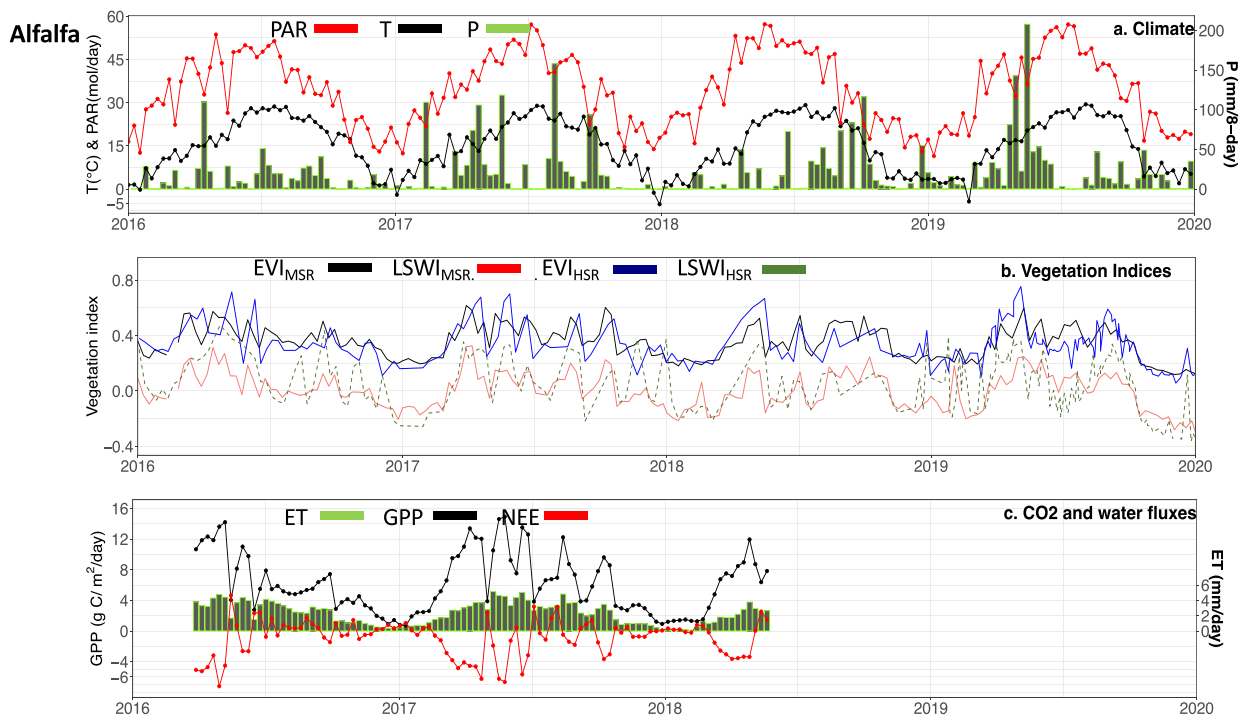


Fig. 3. The seasonal dynamics and interannual variation of climate, vegetation indices, carbon and water fluxes from the alfalfa site. a.) Air temperature(T), photosynthetically active radiation (PAR), and precipitation. T and PAR are 8-day mean values, and precipitation is 8-day sum values. b.) Vegetation indices (enhanced vegetation index (EVI) and land surface water index (LSWI)) derived from MODIS at the 8-day interval and Landsat-Sentinel2. c.) NEE_{EC}, GPP_{EC}, and ET_{EC}.

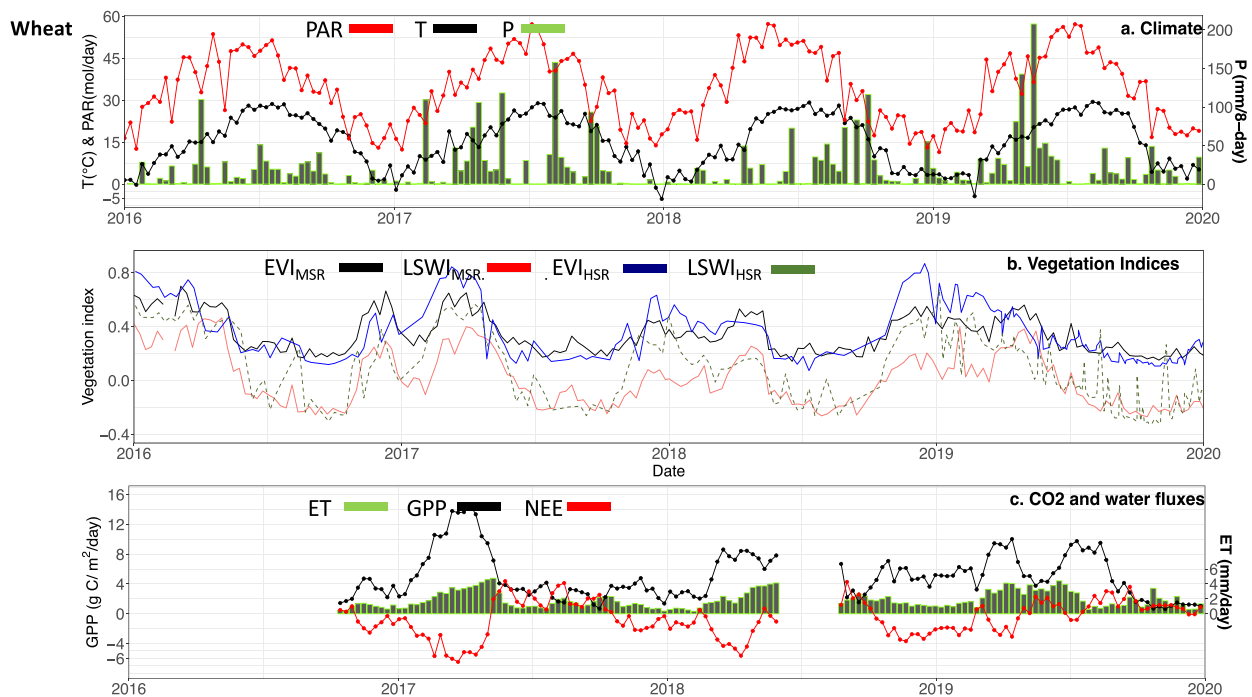


Fig. 4. The seasonal dynamics and interannual variation of climate, vegetation indices, carbon and water fluxes from the winter wheat site. a.) Air temperature(T), photosynthetically active radiation (PAR), and precipitation. T and PAR are 8-day mean values, and precipitation is 8-day sum values. b.) Vegetation indices (enhanced vegetation index (EVI) and land surface water index (LSWI)) derived from MODIS at the 8-day interval and Landsat-Sentinel2. c.) NEE_{EC}, GPP_{EC}, and ET_{EC}.

hand, LSWI derived from MODIS data has higher sensitivity than LSWI_{HSR} for this field. Finally, VIs from both timeseries of optical data provided similar representation of the field seasonality.

At the winter wheat site, seeds were sown in September/October (depending on the purpose of wheat – graze or grain-only) of the previous year, and crops were harvested in early June. Accordingly, the

vegetation index data reflected the crop plant dynamics, including germination in the fall, rapid growth before becoming dormant in winter, and rapid growth in spring after temperatures rise (Fig. 4b). The GPP_{EC} and NEE_{EC} were larger in the spring of 2017 (due to more rainfall) than in the spring of 2018 and 2019 (Fig. 4c). The MSR and HSR vegetation indices captured well SOS and EOS for this winter crop. VIs derived using the HSR data followed more closely the GPP_{EC} and NEE_{EC} seasonal changes, and while both MSR and HSR EVI had similar magnitudes, $LSWI_{HSR}$ exhibited constantly higher values than $LSWI_{MSR}$.

3.2. Relationships between GPP_{EC} and vegetation indices derived from images at moderate (MODIS) and high (Landsat and Sentinel-2) spatial resolutions

At the tallgrass prairie site (Fig. 5a), GPP_{EC} had a stronger linear relationship with the EVI derived from the Landsat/Sentinel-2 images ($R^2 = 0.84$) than from the MODIS images ($R^2 = 0.75$). At the alfalfa site (Fig. 5b), the linear regression model indicated a stronger linear relationship between GPP_{EC} and EVI from Landsat/Sentinel-2 images (0.80) than between GPP_{EC} and EVI from MODIS images (0.73). Finally, the smallest site, the winter wheat site (Fig. 5c) had the weakest linear relationships of all sites. The EVI from Landsat/Sentinel-2 was more strongly correlated with GPP_{EC} ($R^2=0.73$) than did the EVI from the MODIS ($R^2= 0.60$). The comparison between GPP_{EC} and EVI from Landsat/Sentinel-2 and MODIS images demonstrates the importance of using high spatial resolution of satellite images (Landsat/Sentinel-2), owing to mixed pixels for the MODIS.

3.3. Relationships between air temperature, GPP_{EC} , and EVI

We investigated the relationships between EVI, GPP_{EC} , and daily daytime mean air temperature for prairie (Fig. 6a,d), alfalfa (Fig. 6b,e), and winter wheat (Fig. 6c,f) to identify the site-specific optimal air temperature ($T^{opt-site}$) for the VPM simulations. At the native prairie site, GPP_{EC} rose after air temperature reached 10 °C and reached a plateau at around 24 °C. Similarly, the EVI from Landsat/Sentinel-2 and MODIS images rose rapidly after air temperature went up to 10 °C and peaked at around 22 °C. At the alfalfa site, GPP_{EC} increased rapidly after

air temperature was above 10 °C and reached a plateau at around 18 °C. The EVI derived from MODIS and Landsat/Sentinel-2 increased as air temperature rose and peaked at around 22 °C. At the winter wheat site, GPP_{EC} rose after the air temperature was above 2.5 °C and reached a plateau at around 19 °C. Similarly, the EVI from Landsat/Sentinel-2 and MODIS were positive when the air temperature was above 1 °C and reached a plateau at around 19 °C.

Based on the canopy physiological analyses of GPP_{EC} and daily daytime mean air temperature at these three sites, and the observed consistency between GPP_{EC} -temperature and EVI-temperature relationships, we set the T^{opt} value for the VPM simulations as 22 °C for the native prairie, 22 °C for alfalfa, and 19 °C for winter wheat. The consistency between the GPP_{EC} -temperature and EVI-temperature relationships at these sites opens the opportunity to use the EVI-temperature relationship to estimate T^{opt} in other sites without GPP_{EC} data.

3.4. A comparison of EC-derived GPP estimates (GPP_{EC}) and VPM simulations (GPP_{VPM}) using images at moderate (MODIS) and high (Landsat and Sentinel-2) spatial resolutions

The seasonal dynamics of GPP_{VPM} estimates were compared against the seasonal changes of GPP_{EC} (Fig. 7). At the native prairie site, GPP values typically rose in March after the beginning of the vegetation greening and peaked in May with daily carbon uptake >14 g C/m²/day in 2016 and 10 g C/m²/day in 2018. The GPP_{VPM} captured the seasonal dynamics of GPP_{EC} well in terms of SOS and EOS. The $GPP_{VPM-MOD09}$ was overestimated in May-June (during peak growth) of 2018 and 2019. In contrast, the $GPP_{VPM-LS2}$ tracked the seasonal variability of GPP_{EC} better (Fig. 7a).

For the alfalfa site, GPP typically rose after mid-February and reached over 14 g C/m²/day in May during 2016 and 2017, and 12 g C/m²/day in April during 2018. The year 2017, the wettest year, had the largest annual GPP values, with several periods with high GPP (>12 g C/m²/day) in early April, late June, and mid-August. The GPP_{VPM} tracked the seasonality (including peak values and abrupt changes due to hay harvests) of GPP_{EC} well in all years. In addition, Fig. 8b showed that $GPP_{VPM-MOD09}$ was able to track the largest magnitude of GPP_{EC} in 2016.

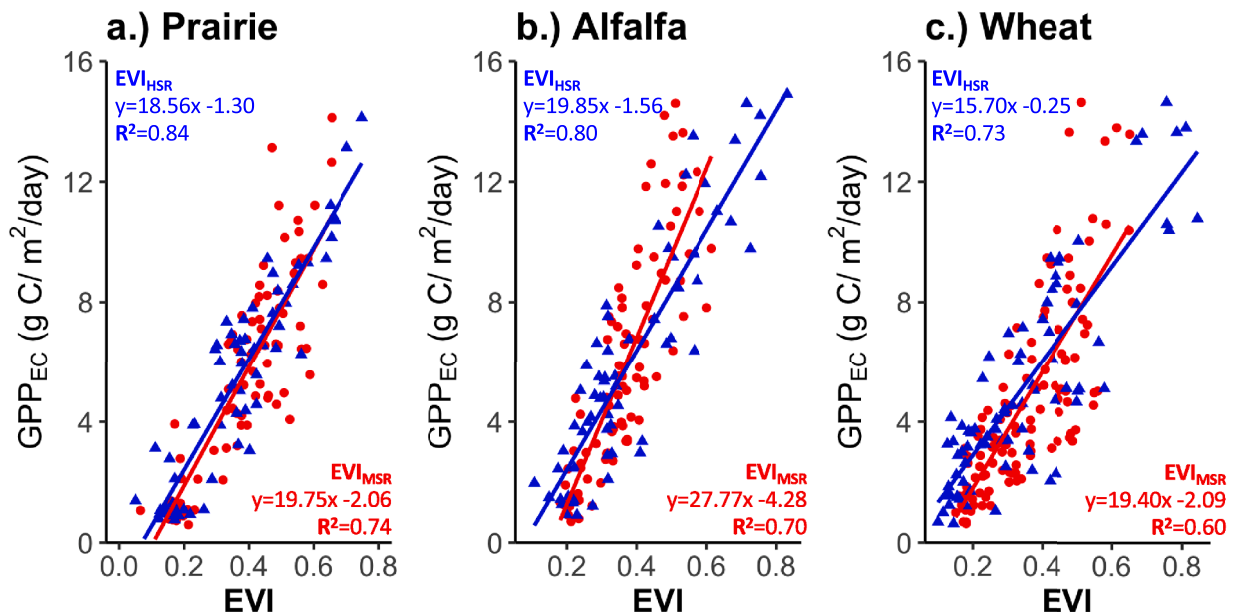


Fig. 5. The relationships between eddy covariance-derived gross primary production (GPP_{EC}) and enhanced vegetation index (EVI) derived from Landsat/Sentinel-2 images at high spatial resolution (blue triangles) and MODIS images at moderate spatial resolution (red dots) at the tallgrass prairie, alfalfa, and winter wheat sites.

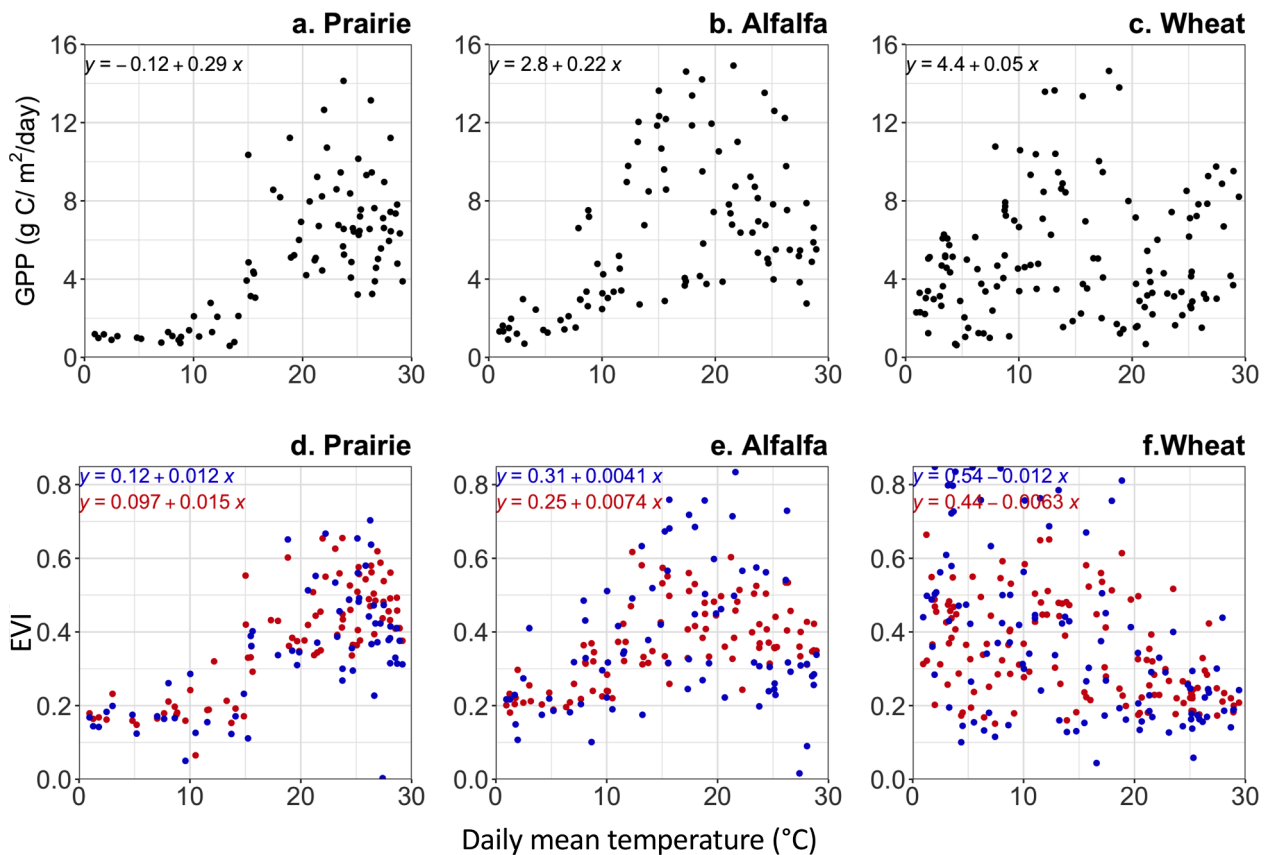


Fig. 6. The relationships between air temperature and GPP_{EC} (upper row a,b, and c) and EVI (lower row d,e, and f) at the tallgrass prairie, alfalfa, and winter wheat sites. Blue dots represent EVI from Landsat/Sentinel-2 at high spatial resolutions, and red dots are EVI from MODIS at moderate spatial resolution.

For the winter wheat site, GPP rose in January. The year 2017 (the wettest year) had the highest GPP_{EC} values, with $>13 \text{ g C/m}^2/\text{day}$ in March and peak GPP_{EC} values of $\sim 15 \text{ g C/m}^2/\text{day}$ in April. The seasonality and these peak values were well captured by the $GPP_{VPM-LS2}$. In 2019, GPP_{EC} peaked in March-April with $GPP >10 \text{ g C/m}^2/\text{day}$ and again in July-August with similar values after significant pluvial events. The second peak (July-August) displayed abnormally high GPP_{EC} values that don't correspond well with the low NEE and ET magnitudes (Fig. 4c.) and the vegetation cover of the field given that it was fallow (no wheat, but some weeds, mainly C4 pigweeds (*Amaranthus spp.*) were present (Fig. S1). All the other seasonal dynamics of GPP_{EC} corresponded well with the NEE magnitudes, and they were captured and represented well by the VPM predictions. The smaller magnitudes of NEE and ET_{EC} , compared to larger magnitudes of GPP_{EC} during the fallow period in the summer of 2019 indicate a flux partitioning error.

The scatterplots of GPP_{EC} and GPP_{VPM} at HSR and MSR showed a strong linear relationship between GPP_{EC} and GPP_{VPM} for these C3 crops and C4 prairie (Fig. 8). The $GPP_{VPM-LS2}$ predictions showed higher correlations with GPP_{EC} than did the $GPP_{VPM-MOD09}$ predictions at the three sites.

3.5. The relationship between EC-measured ET (ET_{EC}) and transpiration estimates from VTM simulations (T_{VTM})

We evaluated the seasonal dynamics of ET_{EC} and T_{VTM} at the three sites (Fig. 9). Peak ET_{EC} values during the plant growing season were similar among the three sites, in the range of 4 to 5 mm/day. However, T_{VTM} in the C4-dominated tallgrass prairie site was substantially lower than T_{VTM} in the C3 alfalfa and winter wheat sites. For the three sites, the ET_{EC}/P ratio and T/ET_{EC} ratio were higher in the drier years (2016 and 2018) compared to the wetter years (2017 and 2019) (Table 2). Fig. 9 and Table 1 display the results of the T_{VTM} estimates derived using

GPP_{EC} (T_{VTM-EC}), $GPP_{VPM-LS2}$ ($T_{VTM-LS2}$), and $GPP_{VPM-MOD09}$ ($T_{VTM-MOD09}$). In the tallgrass prairie site, the seasonal dynamics of T_{VTM} agreed with the seasonal dynamics of ET_{EC} . However, the magnitudes of T_{VTM} were substantially smaller than ET_{EC} during the plant growing season, ranging from 1 to 2 mm/day, accounting for only 45 % (T_{VTM-EC}) of ET_{EC} . The $T_{VTM-LS2}$ and T_{VTM-EC} displayed similar results with low variability ($<3 \%$) among their annual totals, while the $T_{VTM-MOD09}$ estimates were 30 % higher than T_{VTM-EC} .

At the alfalfa site, the seasonal dynamics of T_{VTM} corresponded well with the ET_{EC} time series and tracked the reduction in T after hay harvest events. The T_{VTM} was substantially lower than ET_{EC} after hay harvests. Both ET_{EC} and T_{VTM} peak values ranged between 4 and 5 mm/day. During the growing season, $T_{VTM-LS2}$ and T_{VTM-EC} accounted for 67 % and 92 % of ET_{EC} , respectively. The annual total estimates of $T_{VTM-LS2}$ were lower than T_{VTM-EC} , while $T_{VTM-MOD09}$ had closer annual total values to T_{VTM-EC} .

At the winter wheat site, T_{VTM} tracked the seasonal dynamics of ET_{EC} well from late 2016 to early 2019. We observed the highest ET_{EC}/P ratio (86 %) in 2018. The lowest T_{VTM}/ET_{EC} ratios were observed in 2019, with 39 % ($T_{VTM-LS2}$), 50 % ($T_{VTM-MOD09}$), and 79 % (T_{VTM-EC}).

Table 2 shows the differences between total rainfall (P) and ET_{EC} , total T_{VTM} from GPP_{EC} , T_{VTM-EC} from $GPP_{VPM-LS2}$, and T_{VTM-EC} from $GPP_{VPM-MOD09}$. Table 2 shows higher ET/P ratios during the drier year (2016 and 2018).

4. Discussion

4.1. Biophysical performance of vegetation indices from MSR (MODIS) and HSR (Landsat and Sentinel-2) at C3 annual crop sites and C4-dominant perennial prairie

The combined use of Landsat and Sentinel-2 (HSR images) to

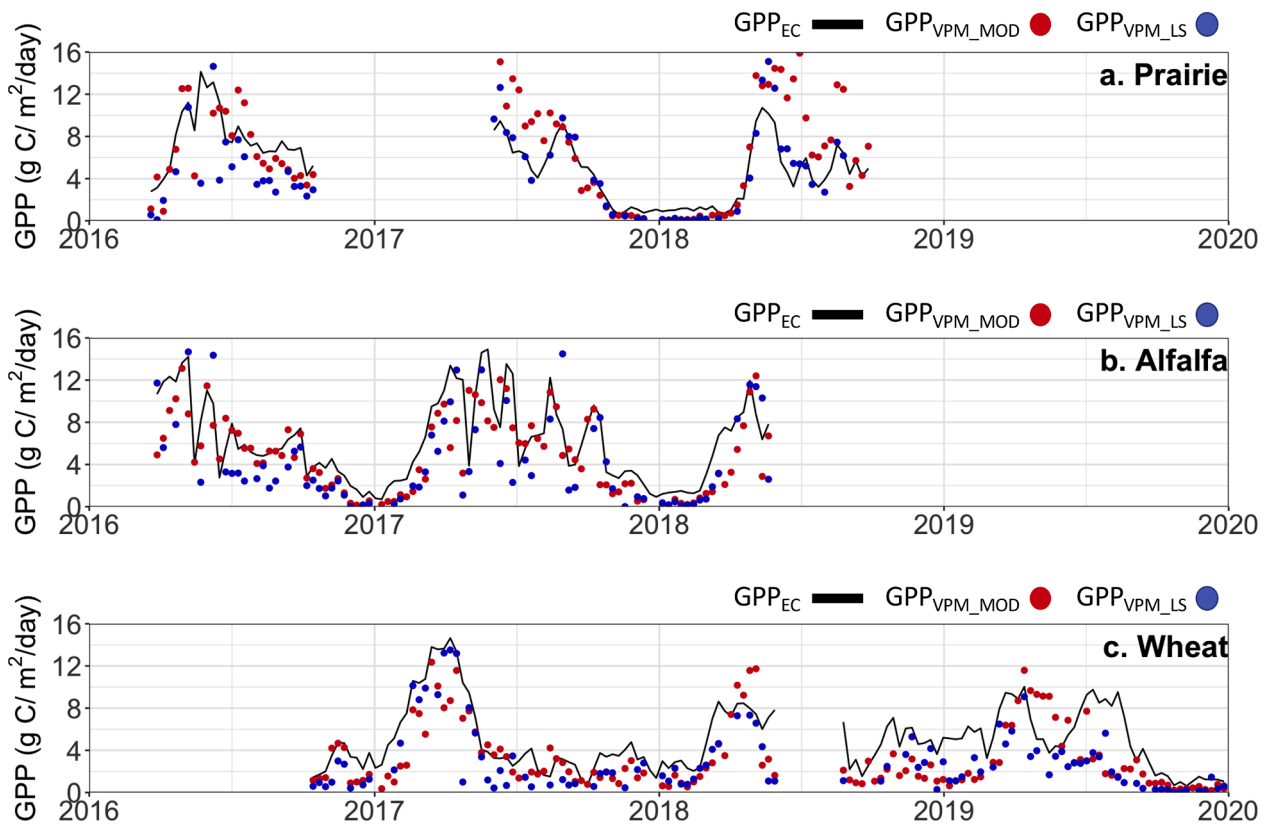


Fig. 7. Seasonal dynamics of predicted and eddy covariance-derived gross primary production (GPPVPM and GPPEC) at the tallgrass prairie, alfalfa, and winter wheat sites.

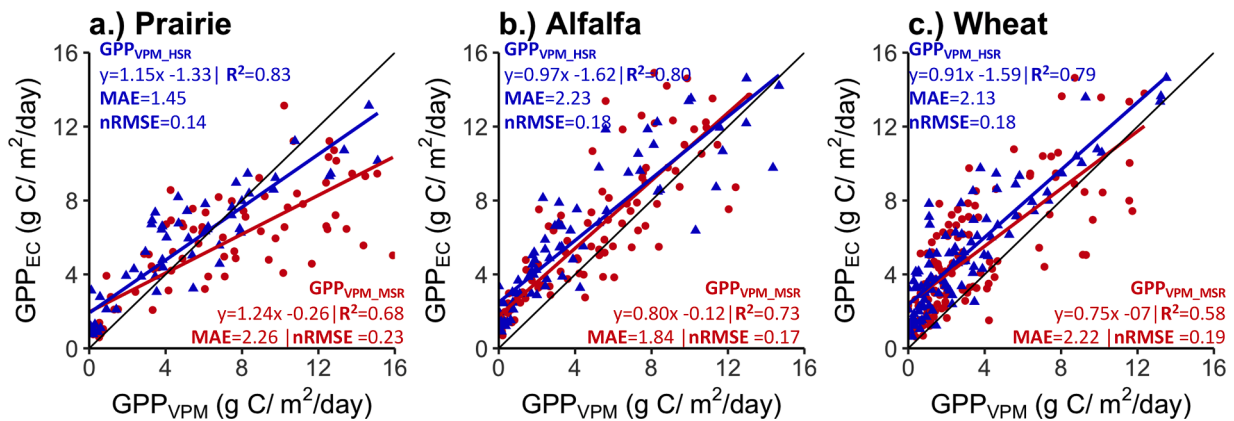


Fig. 8. Comparison between predicted and estimated GPP (GPP_{VPM} and GPP_{EC}) at the tallgrass prairie, alfalfa, and winter wheat sites.

construct time series of VIs data helped to overcome the limitations of data frequency and enabled to effectively track the seasonal dynamics of vegetation canopy for the native prairie, alfalfa, and wheat sites. This underscores the necessity of integrating multiple HSR optical data sources for consistent and effective crop phenology monitoring. This aligns with findings from Griffiths et al. (2019), which highlights the need of 10-day Landsat-Sentinel2 composites for precise agricultural mapping in Germany, and Li & Roy (2017) that emphasizes the importance of combined Landsat-Sentinel data to generate cloud-free data for landcover change studies and continuous monitoring of ecosystems at a global scale. Additional studies such as (Liu et al., 2020; Zhang et al., 2022) also underline the importance of this combined data approach to address HSR limitations, particularly in representing interannual crop intensity variations in regions like China and Southern Africa. Notably,

while Landsat and Sentinel-2 images have a coarser temporal resolution (16-day revisit for Landsat and 5-day revisit for Sentinel-2A/B), cloud coverage conditions can introduce additional data gaps. Relying on a single satellite may not yield continuous observations sufficient to track the temporal changes in vegetation canopy. However, in this study merging Landsat and Sentinel-2A/B imagery increased the number of good-quality observations, ensuring more continuous data to track the land surface phenology at the three study locations.

Time series images from the MODIS sensors (MSR images) with 1–2 days of revisit time can track the seasonal dynamics and interannual variations of land surface phenology (Ganguly et al., 2010; Xiao et al., 2005; Xiao et al., 2004, 2005; Zurita-Milla et al., 2009). However, our study sites were small and contained mixed pixels for the MODIS (~500 m resolutions). As a result, we observed stronger relationships of the EVI

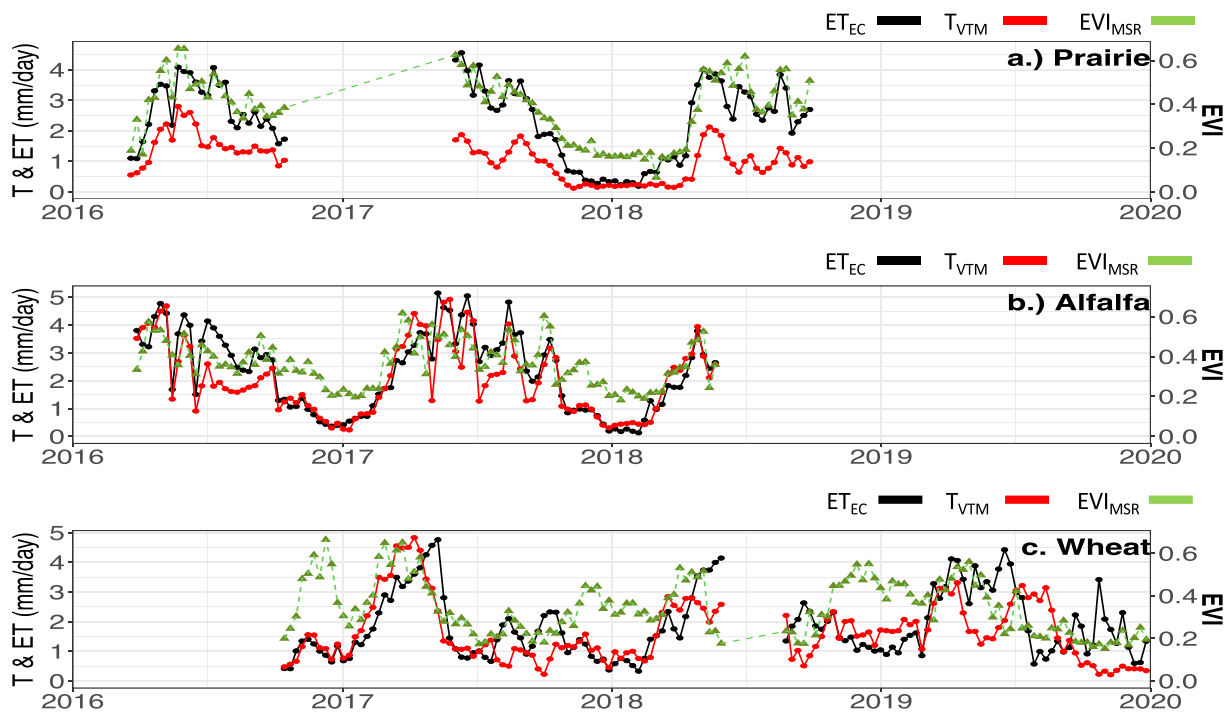


Fig. 9. Seasonal dynamics of 8-day daily average predicted (ET_{T-VTM}), 8-day EVI_{MSR} , and eddy covariance measured evapotranspiration (ET_{EC}) at the tallgrass prairie, alfalfa, and winter wheat sites.

Table 1

A comparison of annual precipitation, evapotranspiration (ET_{EC}) from the tower observation, and transpiration (T_{VTM}) from Vegetation Transpiration Model simulations at the tallgrass prairie, alfalfa pasture, and winter wheat sites. Daily ET_{EC} ($mm\ day^{-1}$) and T_{VTM} ($mm\ day^{-1}$) from the study sites were aggregated over those days with ET observations.

	Year	Annual totals (mm)				
		P	ET_{EC}	T_{VTM-EC}	$T_{VTM-LS2}$	$T_{VTM-MOD09}$
Prairie	2016	517	488	272	153	317
	2017	527	340	141	143	257
	2018	476	442	170	166	328
Alfalfa	2016	542	582	458	330	477
	2017	1108	721	660	437	611
	2018	147	166	178	137	158
Wheat	2017	1109	619	568	401	421
	2018	556	476	442	284	370
	2019	1084	755	599	298	376

Table 2

A comparison of the ratio of annual evapotranspiration (ET_{EC}) from tower observation to annual precipitation (P), and the ratio of different transpiration (T_{VTM}) estimates from Vegetation Transpiration Model to ET_{EC} at the tallgrass prairie, alfalfa pasture, and winter wheat sites. Daily ET_{EC} ($mm\ day^{-1}$) and T_{VTM} ($mm\ day^{-1}$) from the study sites were aggregated over those days with ET observations for the study period within each year.

	Year	Study period water return rates (%)			
		$ET_{EC}:P$	$T_{VTM-EC}:ET_{EC}$	$T_{VTM-LS2}:ET_{EC}$	$T_{VTM-MOD09}:ET_{EC}$
Prairie	2016	94	56	31	65
	2017	65	41	42	76
	2018	93	38	38	74
Alfalfa	2016	107	79	57	82
	2017	65	92	61	85
	2018	113	107	83	95
Wheat	2017	56	92	65	68
	2018	86	93	60	78
	2019	70	79	39	50

from Landsat/Sentinel-2 images (EVI_{HSR}) than from the MODIS images (EVI_{MSR}) with GPP_{EC} . The higher spatial resolution of EVI_{HSR} offered a more granular depiction of vegetation characteristics such as structure, health, and phenological stages, which aligned more closely with GPP data from the eddy flux tower sites. This finding is consistent with other research (Brown et al., 2007; Lin et al., 2019; Wagle et al., 2020), underscoring the advantages of using high-spatial-resolution EVI products to establish stronger relationships with CO_2 fluxes. This is primarily attributed to the improved congruence between the tower footprint and the pixels in high-spatial-resolution remote sensing images. The results show that the EVI and LSWI were effective in tracking the land surface phenology (SOS and EOS) of prairie, alfalfa, and winter wheat. The LSWI was able to delineate the harvest dates and detect field disturbances (i.e., tillage) with a lower sensitivity to these events when derived using the MSR indexes. Our results show that the temporal consistency of the land surface phenology metrics derived from the VI-based and GPP_{EC} -based approaches correspond well with the field management and seasonal dynamics of vegetation. The VI-based approach showed higher sensitivity to small field disturbances, while both approaches effectively captured the management practices, SOS, and EOS well for the three sites. The EVI_{HSR} displayed higher accuracy and sensitivity to the changes in canopy structure and crop development than the EVI_{MSR} at the three sites. The highest difference between the two observations was observed for the winter wheat, where optical data had challenges representing the magnitude of plant biomass increase due to flowering and development of wheat grain heads. Moreover, additional uncertainty can be attributed to the proximity to other winter wheat fields that had different management practices. The MODIS pixels of 500 m (MSR) are often mixed in croplands, while Landsat and Sentinel-2 images represent pure pixels. This difference can contribute to larger differences in the relationships of GPP_{EC} with EVI_{MSR} and EVI_{HSR} in smaller winter wheat fields (Meng et al., 2013; Ozdogan and Woodcock, 2006; Wardlow et al., 2007).

Our findings indicate that in addition to GPP , vegetation greenness (e.g., EVI) provides a reasonable option to determine the site-specific optimal temperature in tallgrass prairie, alfalfa pasture, and winter

wheat sites where ground-based GPP_{EC} data are not available. Finally, the results demonstrate the impact of using MSR and HSR-derived vegetation indices at the field level, which are important for estimating crop performance and vegetation health insurance indices over farms with multiple crops, rotations, and management practices (Bokusheva et al., 2016; Kogan et al., 2012; Wagle et al., 2020).

4.2. Comparison of GPP estimates from Landsat/ Sentinel-2 data (HSR) and Modis (MSR) data

The GPP estimates from the VPM simulations using local climate data agreed reasonably well with the GPP_{EC} data. However, $GPP_{VPM-LS2}$ estimates were closer to GPP_{EC} than $GPP_{VPM-MOD}$. This can be attributed largely to two factors: (1) a MODIS pixel often includes multiple crop fields that have different management practices and cultivation calendars, and (2) the footprints of short (i.e., 2–3 m) eddy flux towers in crop fields are much smaller than the size of a MODIS pixel (500 m). Similar limitations of using MODIS images have been reported in previous studies (Balzarolo et al., 2019; Gitelson et al., 2008; Zhu et al., 2020). In comparison, vegetation indices from Landsat and Sentinel-2 images, which are used to calculate $fPAR_{chl}$ and W_{scalar} , often reflect the vegetation canopy dynamics from one crop field within the footprint of the eddy flux tower (Skakun et al., 2017; Wolanin et al., 2019). The results from this study highlight the potential of VPM for estimating GPP in C3 vegetation and C4-dominated fields using Landsat and Sentinel-2 images. The GPP simulation results showed that $GPP_{VPM-MOD}$ estimates had the strongest linear relationship with GPP_{EC} in the alfalfa field, which was the largest field of the three studied sites (the MODIS pixel was mostly within the alfalfa field). The weakest linear relationship between $GPP_{VPM-MOD}$ and GPP_{EC} estimates was observed in the winter wheat site, which was the smallest field. The wheat field was small (28 ha) and the MODIS pixel included neighboring wheat fields with different management practices.

The sources of errors and uncertainties of GPP estimates from the LUE-based models include model structure, model parameters, and input datasets including satellite images and climate data. The comparison of VPM simulations between MSR and HSR images illustrates the error source and uncertainty associated with land cover types within one image pixel and the spatial mismatch (inconsistency) between the image pixel and the footprints of eddy flux towers (Ran et al., 2016; Zheng et al., 2018). One of the limitations of MSR satellite data is that one MSR pixel often contains multiple land cover types, often called a mixed pixel, while one HSR pixel most likely contains one land cover type, often called a pure pixel (Brown et al., 2007; He et al., 2017; Yu et al., 2018). The presence of different landcover types within a single pixel affects the model's representation of the fraction of PAR absorbed by the chlorophyll and the vegetation water response, which are strong drivers of vegetation carbon uptake. Moreover, the quality of the data from satellite optical sensors decreases with cloud conditions and the cloud coverage limitations have a large impact on HSR data, reducing the continuity in time series data. In addition, the EC-flux tower estimates will be influenced by the surrounding fields as tower footprint changes with the season, weather conditions, vegetation height, and vegetation cover (Celis et al., 2021; Kijun et al., 2015; Ran et al., 2016). The source of uncertainty in EC measurements and flux partitioning (NEE into GPP and ER) errors also increases the challenges to validate GPP estimates.

4.3. Capacity of VTM in estimating daily t in C3 wheat and alfalfa, and C4-dominated native prairie

The daily T estimates from the VTM closely followed the seasonal dynamics of ET_{EC} , showing that T_{VTM} could be used as an indicator of water use and water stress, given the importance and advantages of quantifying T in different land use types (Angus and Van Herwaarden, 2001; Bremer et al., 2001; Condon et al., 2002; Miao et al., 2016).

The prairie site had an average of 84 % of precipitation (P) returned

to the atmosphere through ET_{EC} during the study period with higher values in periods of dry years (<90 % in 2016) and lower rates in periods of wet years (~60 % in 2017), being consistent with the ET rates reported in other studies (Burba and Verma, 2005) for this ecosystem in Oklahoma. Annual T:ET rates determined using VTM were similar to values reported in other C4-dominated native prairie (O'Keefe et al., 2020), having a consistent values range using T_{VTM-EC} (45 %) and $T_{VTM-LS2}$ (37 %) estimates for our study period. Nonetheless, $T_{VTM-MOD09}$ (71 %) had the largest T rate, and this higher rate difference can be partially explained given the spatial resolution (500 m) of this product and the presence of other pastures and small sections of trees within the pixel (Fig. 1). The different management regimes of pastures and C3:C4 vegetation composition directly impact E losses as well as T rates in prairie systems (Bajgain et al., 2018; Logan and Brunsell, 2015; Wagle et al., 2017).

Substantially smaller T estimates by VTM for this C4-dominated tallgrass prairie site than C3 alfalfa and winter wheat sites in this study can be attributed to the use of higher WUE (C4 parameterization) value for tallgrass prairie. However, GPP and ET magnitudes were similar in these three ecosystems (Bajgain et al., 2018; Wagle et al., 2019a,b). Furthermore, Bajgain et al. (2018) reported higher WUE in winter wheat than in tallgrass prairie. Studies use the same WUE parameters for all C4 species for modeling purposes, regardless of differences in species types (e.g., grasses vs. crops), management practices (e.g., rainfed vs. irrigated), and productivity. For example, the maximum GPP can be 28–30 g C/m²/day in irrigated maize (*Zea mays* L.) in Nebraska (Suyker and Verma, 2010), which is 2–3 times bigger than those observed in tallgrass prairie. Using the same C4 WUE parameter, VTM would estimate 2–3 times bigger T for the irrigated maize than tallgrass prairie as T is simply estimated by the ratio of GPP to WUE in VTM. The results of this study underline some potentials as well as limitations of this VTM approach given some of the challenges to account for the discrepancies between GPP and WUE estimates. Thus, additional parameterization may be needed to improve its performance in accurately predicting field-level T patterns across different species types, management practices, and productivity levels. In the alfalfa field, a comparison of cumulative P and cumulative ET_{EC} during the study period revealed that the field's ET_{EC} totals were higher than P totals in drier years (2016 and 2018). Alfalfa's deep root systems can withdraw water from deeper depths during dry conditions. Pluvial events during March–April 2016 just before the study was initiated also contributed to a higher initial soil moisture condition and subsequent higher ET flux rates in this site (Wagle et al., 2020). T estimates by VTM were consistent with the expected higher T rate for alfalfa, which has rapid increase and growth after events like grazing or harvesting (Irmak et al., 2003; Shi et al., 2017; Wagle et al., 2020). However, for the 2016–2017 study period, the 10 m transpiration estimates ($T_{VTM-LS2}$) had the lowest rate (60 %) of the annual ET_{EC} flux, while $T_{VTM-MOD09}$ (500 m) constituted 82 %, being closer to the T_{VTM-EC} (EC fetch footprint - ~100 m) estimates that accounted for 85.5 % of ET_{EC} . The VTM results indicate that for a larger field like the alfalfa site (48 ha), one single HSR pixel does not provide a significant representation of the water flux variability across the entire field, which might present different biogeochemical and soil moisture dynamics as discussed in multiple studies (Joshi et al., 2011; Logan and Brunsell, 2015). Furthermore, our T_{VTM-EC} and $T_{VTM-MOD09}$ results demonstrate the strength and potential of VTM given consistency in magnitude with the T:ET values reported for this alfalfa field during the 2016–2017 growing season (81 %) (Wagle et al., 2020) using the Flux Variance Similarity ET partitioning method.

For the winter wheat site, annual ET_{EC} accounted for 55 %, 85 %, and 69 % of the total P in 2017, 2018, and 2019, respectively. The T_{VTM-EC} estimates represented the highest T:ET ratios of 91 %, 92 %, and 79 %, respectively, of the annual ET_{EC} . The data anomaly in GPP_{EC} estimates for the second part (i.e., fallow period) of the 2019 year (Fig. 4c and Fig. S1) introduced direct bias into the T_{VTM-EC} estimates. For simplicity, we used the C3 WUE value to estimate T for the entire study period for

winter wheat, but the fallow period had a small presence of C4 pigweeds with abnormally high GPP_{EC} values, resulting in higher T values than ET. Since VTM estimates T solely based on GPP and WUE estimates, these WUE and GPP estimates need to be accurate to successfully capture the water flux dynamics using the VTM model. Some of the uncertainty in T_{VTM-EC} for other periods can be partially attributed to the variability of the fetch footprint (Kljun et al., 2015; Ran et al., 2016), which can have stronger variations depending on the location of the EC system and the landcover changes of the neighboring fields. The $T_{VTM-MOD09}$ estimates (68 %, 78 %, and 50 % of ET_{EC}) were higher than the $T_{VTM-LS2}$ estimates (65 %, 60 %, and 39 % of ET_{EC}) for 2017, 2018, and 2019. Larger $T_{VTM-MOD09}$ estimates typically are linked with the heterogeneity of MODIS pixel size as this has been shown to contribute to overestimations of carbon and water fluxes in crops like winter wheat (Yang et al., 2014). Nevertheless, both MSR and HSR VTM estimates kept a transpiration flux magnitude consistent with the values found in other studies (Bajgain et al., 2018; Wu et al., 2011), representative of a more efficient water use capacity in winter wheat crops. These results demonstrate the benefits of using a model like VTM, which is fed with satellite products at different spatial resolutions, to represent T. This is because VTM is sensitive to field management events and field conditions, which can impact T rates (Morison and Gifford, 1984; Vadez et al., 2014).

5. Conclusions

In this study, we investigated the potential of HSR Landsat and Sentinel-2 images, along with MSR MODIS images, to track the phenology and GPP of C3 winter wheat and alfalfa, and a C4-dominated native prairie in Oklahoma, USA. The analysis between GPP_{EC} , EVI, and air temperature provided new insights into the biophysical performance of vegetation indices and a reasonable method for determining the optimum air temperature at individual sites. This could lead to a better understanding of the effects of air temperature on photosynthesis. The results show that the VPM performed well in estimating the seasonal dynamics of GPP at the three sites and HSR $GPP_{VPM-LS2}$ agreed more strongly with GPP_{EC} than did MSR $GPP_{VPM-MOD}$. The analyses of GPP_{EC} from the EC flux tower sites and GPP_{VPM} with in-situ climate data and remote sensing data (HSR and MSR) show the capacity of the VPM to estimate and predict GPP of C3 and C4 ecosystems in Oklahoma using remote sensing observations at moderate and high spatial resolutions.

The results show that the VTM effectively tracked the seasonal dynamics of ET in prairie, alfalfa, and winter wheat. However, additional parameterization may be needed for this simple VTM approach to accurately estimate field-level T patterns across different species types, management practices, and productivity levels. The use of GPP_{VPM} estimates to calculate T_{VTM} offers a simpler way to represent the water use in C3 crops and C4-dominated prairie. The information provided in our study demonstrates the necessity and potential of using Landsat and Sentinel-2 images for the study of phenology and estimates of GPP and T in tallgrass prairie, alfalfa, and winter wheat. Further assessment of VPM and VTM at other C3 agroecosystems and C4-dominated native prairie fields with EC flux tower sites is still needed, including those with irrigation practices. This would help us to better understand the potential sources of uncertainty in the simulations and representation of the carbon and water fluxes.

Declaration of Competing Interest

The authors declare that they have no known competing financial interests or personal relationships that could have appeared to influence the work reported in this paper.

Data availability

Data will be made available on request.

Acknowledgements

This study was supported in part by grants from the USDA National Institute of Food and Agriculture (NIFA, 2016-68002-24967), the US National Science Foundation (1946093), the NASA GeoCarb Mission (GeoCarb Contract No. 80LARC17C0001), and the USDA-ARS (Project number: 3070-21610-003-00D).

Credit author statement

Mr. Celis: Led the modeling components for the VPM and VTM models. Conducted background research, processed satellite data, and spearheaded the results and analysis sections.

Conceived the study idea, analyzed data, and wrote the manuscript.

Dr. Wagle: Processed the eddy covariance (EC) data and collaborated with Dr. Xiao on the introduction, results, analysis, and conclusions. Provided expertise on the eddy covariance towers data, agronomy of the fields, and the assessment of transpiration and ET. Conceived the study idea, reviewed the manuscript, and provided intellectual input.

Dr. Xiao: Supported the modeling and remote sensing components. Conceived the study idea, reviewed the manuscript, and provided intellectual input.

Dr. Basara: Assisted with the weather data analysis and methodology.

Dr. McCarthy and Dr. Souza: Contributed insights on plant biophysics and photosynthetic traits.

All authors collaboratively reviewed the manuscript and provided valuable intellectual input.

Supplementary materials

Supplementary material associated with this article can be found, in the online version, at [doi:10.1016/j.agrformet.2023.109797](https://doi.org/10.1016/j.agrformet.2023.109797).

References

- Ai, Z., Wang, Q., Yang, Y., Manevski, K., Yi, S., Zhao, X., 2020. Variation of gross primary production, evapotranspiration and water use efficiency for global croplands. *Agric. For. Meteorol.* 287, 107935.
- Alfieri, J.G., Xiao, X., Niyogi, D., Pielke, R.A., Chen, F., LeMone, M.A., 2009. Satellite-based modeling of transpiration from the grasslands in the Southern Great Plains, USA. *Glob Planet Change* 67 (1), 78–86. <https://doi.org/10.1016/j.gloplacha.2008.12.003>.
- Allen, R.G., Tasumi, M., Trezza, R., 2007. Satellite-based energy balance for mapping evapotranspiration with internalized calibration (METRIC)—Model. *J. Irrig. Drain. Eng.* 133 (4), 380–394.
- Anav, A., Friedlingstein, P., Beer, C., Ciais, P., Harper, A., Jones, C., Murray-Tortarolo, G., Papale, D., Parazoo, N.C., Peylin, P., 2015. Spatiotemporal patterns of terrestrial gross primary production: a review. *Rev. Geophys.* 53 (3), 785–818.
- Angus, J.F., Van Herwaarden, A.F., 2001. Increasing water use and water use efficiency in dryland wheat. *Agron. J.* 93 (2), 290–298.
- Bajgain, R., Xiao, X., Basara, J., Wagle, P., Zhou, Y., Mahan, H., Gowda, P., McCarthy, H. R., Northup, B., Neel, J., Steiner, J., 2018. Carbon dioxide and water vapor fluxes in winter wheat and tallgrass prairie in central Oklahoma. *Sci. Total Environ.* 644, 1511–1524. <https://doi.org/10.1016/j.scitotenv.2018.07.010>.
- Balzarolo, M., Peñuelas, J., Veroustraete, F., 2019. Influence of landscape heterogeneity and spatial resolution in multi-temporal In Situ and MODIS NDVI data proxies for seasonal GPP dynamics. *Remote Sens. (Basel)* 11 (14). <https://doi.org/10.3390/rs11141656>. Article 14.
- Barrett, C.B., 2021. Overcoming global food security challenges through science and solidarity. *Am. J. Agric. Econ.* 103 (2), 422–447. <https://doi.org/10.1111/ajae.12160>.
- Beer, C., Reichstein, M., Tomelleri, E., Ciais, P., Jung, M., Carvalhais, N., Rödenbeck, C., Arain, M.A., Baldocchi, D., Bonan, G.B., 2010. Terrestrial gross carbon dioxide uptake: global distribution and covariation with climate. *Science* 329 (5993), 834–838.
- Ben-Asher, J., Tsuyuki, I., Bravdo, B.-A., Sagih, M., 2006. Irrigation of grapevines with saline water: I. Leaf area index, stomatal conductance, transpiration and photosynthesis. *Agric. Water Manage.* 83 (1), 13–21. <https://doi.org/10.1016/j.agwat.2006.01.002>.
- Bokusheva, R., Kogan, F., Vitkovskaya, I., Conrath, S., Batyrbayeva, M., 2016. Satellite-based vegetation health indices as a criteria for insuring against drought-related yield losses. *Agric. Forest Meteorol.* 220, 200–206. <https://doi.org/10.1016/j.agrformet.2015.12.066>.

- Bremer, D.J., Auen, L.M., Ham, J.M., Owensby, C.E., 2001. Evapotranspiration in a prairie ecosystem. *Agron. J.* 93 (2), 338–348. <https://doi.org/10.2134/agronj2001.932338x>.
- Brown, J.C., Jepson, W.E., Kastens, J.H., Wardlow, B.D., Lomas, J.M., Price, K.P., 2007. Multitemporal, moderate-spatial-resolution remote sensing of modern agricultural production and land modification in the Brazilian Amazon. *Glsci Remote Sens.* 44 (2), 117–148. <https://doi.org/10.2747/1548-1603.44.2.117>.
- Burba, G.G., Verma, S.B., 2005. Seasonal and interannual variability in evapotranspiration of native tallgrass prairie and cultivated wheat ecosystems. *Agric. For. Meteorol.* 135 (1), 190–201. <https://doi.org/10.1016/j.agrformet.2005.11.017>.
- Cabral, O.M., Rocha, H.R., Gash, J.H., Ligo, M.A., Ramos, N.P., Packer, A.P., Batista, E.R., 2013. Fluxes of CO₂ above a sugarcane plantation in Brazil. *Agric. For. Meteorol.* 182, 54–66.
- Campbell, J.E., Berry, J.A., Seibt, U., Smith, S.J., Montzka, S.A., Launois, T., Belviso, S., Bopp, L., Laine, M., 2017. Large historical growth in global terrestrial gross primary production. *Nature* 544 (7648). <https://doi.org/10.1038/nature22030>. Article 7648.
- Celis, J.A. (2019). *Process based modeling of surface energy fluxes, evapotranspiration, soil moisture, and soil temperature in the US Southern Plains*.
- Celis, J.A., Moreno, H.A., Basara, J.B., McPherson, R.A., Cosh, M., Ochsner, T., Xiao, X., 2021. From standard weather stations to virtual micro-meteorological towers in ungauged sites: modeling tool for surface energy fluxes, evapotranspiration, soil temperature, and soil moisture estimations. *Remote Sens. (Basel)* 13 (7). <https://doi.org/10.3390/rs13071271>. Article 7.
- Celis, J., Xiao, X., Basara, J., Wagle, P., McCarthy, H., 2023. Simple and innovative methods to estimate gross primary production and transpiration of crops: a review. *Digital Ecosyst. Innov. Agric.* 125–156.
- Chang, Q., Xiao, X., Doughty, R., Wu, X., Jiao, W., Qin, Y., 2021. Assessing variability of optimum air temperature for photosynthesis across site-years, sites and biomes and their effects on photosynthesis estimation. *Agric. For. Meteorol.* 298–299, 108277. <https://doi.org/10.1016/j.agrformet.2020.108277>.
- Chang, Q., Xiao, X., Wu, X., Doughty, R., Jiao, W., Bajgain, R., Qin, Y., Wang, J., 2020. Estimating site-specific optimum air temperature and assessing its effect on the photosynthesis of grasslands in mid- to high-latitudes. *Environ. Res. Lett.* 15 (3), 034064. <https://doi.org/10.1088/1748-9326/ab70bb>.
- Condon, A.G., Richards, R.A., Rebetzke, G.J., Farquhar, G.D., 2002. Improving intrinsic water-use efficiency and crop yield. *Crop Sci.* 42 (1), 122–131.
- Dong, J., Fu, Y., Wang, J., Tian, H., Fu, S., Niu, Z., Han, W., Zheng, Y., Huang, J., Yuan, W., 2020. Early-season mapping of winter wheat in China based on Landsat and Sentinel images. *Earth Syst. Sci. Data* 12 (4), 3081–3095. <https://doi.org/10.5194/essd-12-3081-2020>.
- Drusch, M., Del Bello, U., Carlier, S., Colin, O., Fernandez, V., Gascon, F., Hoersch, B., Isola, C., Laberinti, P., Martimort, P., 2012. Sentinel-2: ESA's optical high-resolution mission for GMES operational services. *Remote Sens. Environ.* 120, 25–36.
- Du, Y., Teillet, P.M., Cihlar, J., 2002. Radiometric normalization of multitemporal high-resolution satellite images with quality control for land cover change detection. *Remote Sens. Environ.* 82 (1), 123–134. [https://doi.org/10.1016/S0034-4257\(02\)00029-9](https://doi.org/10.1016/S0034-4257(02)00029-9).
- Duchemin, B., Hadria, R., Erraki, S., Boulet, G., Maisongrande, P., Chehbouni, A., Escadafal, R., Ezzahar, J., Hoedjes, J.C.B., Kharrou, H., Khabba, P., Mougnot, B., Olioso, A., Rodriguez, J.-C., Simonneau, V., 2006. Monitoring wheat phenology and irrigation in Central Morocco: on the use of relationships between evapotranspiration, crops coefficients, leaf area index and remotely-sensed vegetation indices. *Agric. Water Manage.* 79 (1), 1–27. <https://doi.org/10.1016/j.agwat.2005.02.013>.
- Foga, S., Scaramuzza, P.L., Guo, S., Zhu, Z., Dilley Jr, R.D., Beckmann, T., Schmidt, G.L., Dwyer, J.L., Hughes, M.J., Laue, B., 2017. Cloud detection algorithm comparison and validation for operational Landsat data products. *Remote Sens. Environ.* 194, 379–390.
- Ganguly, S., Friedl, M.A., Tan, B., Zhang, X., Verma, M., 2010. Land surface phenology from MODIS: characterization of the collection 5 global land cover dynamics product. *Remote Sens. Environ.* 114 (8), 1805–1816. <https://doi.org/10.1016/j.rse.2010.04.005>.
- Gascon, F., Bouzinac, C., Thépaut, O., Jung, M., Francesconi, B., Louis, J., Lonjou, V., Lafrance, B., Massera, S., Gaudel-Vacaresse, A., Languille, F., Alhammoud, B., Viallefont, F., Pflug, B., Bieniarz, J., Clerc, S., Pessiot, L., Trémas, T., Cadau, E., Fernandez, V., 2017. Copernicus sentinel-2A calibration and products validation status. *Remote Sens. (Basel)* 9 (6). <https://doi.org/10.3390/rs9060584>. Article 6.
- Gitelson, A.A., Vina, A., Masek, J.G., Verma, S.B., Stuyker, A.E., 2008. Synoptic monitoring of gross primary productivity of maize using landsat data. *IEEE Geosci. Remote Sens. Lett.* 5 (2), 133–137. <https://doi.org/10.1109/LGRS.2008.915598>.
- Griffiths, P., Nendel, C., Hostert, P., 2019. Intra-annual reflectance composites from Sentinel-2 and Landsat for national-scale crop and land cover mapping. *Remote Sens. Environ.* 220, 135–151. <https://doi.org/10.1016/j.rse.2018.10.031>.
- Guan, K., Berry, J.A., Zhang, Y., Joiner, J., Guanter, L., Badgley, G., Lobell, D.B., 2016. Improving the monitoring of crop productivity using spaceborne solar-induced fluorescence. *Glob Chang. Biol.* 22 (2), 716–726. <https://doi.org/10.1111/gcb.13136>.
- He, A., He, J., Kim, R., Like, D., Yan, A., 2017. An ensemble-based approach for classification of high-resolution satellite imagery of the Amazon Basin. In: 2017 IEEE MIT Undergraduate Research Technology Conference (URTC), pp. 1–4.
- Hlisenikovsky, L., Mensík, L., Kunzová, E., 2023. Development and the effect of weather and mineral fertilization on grain yield and stability of winter wheat following alfalfa—analysis of long-term field trial. *Plants* 12 (6). <https://doi.org/10.3390/plants12061392>. Article 6.
- Huang, M., Piao, S., Ciais, P., Peñuelas, J., Wang, X., Keenan, T.F., Peng, S., Berry, J.A., Wang, K., Mao, J., 2019a. Air temperature optima of vegetation productivity across global biomes. *Nat. Ecol. Evol.* 3 (5), 772–779.
- Huang, X., Liu, J., Zhu, W., Atzberger, C., Liu, Q., 2019b. The optimal threshold and vegetation index time series for retrieving crop phenology based on a modified dynamic threshold method. *Remote Sens. (Basel)* 11 (23). <https://doi.org/10.3390/rs11232725>. Article 23.
- Huete, A.R., Liu, H.Q., Batchily, K.V., Van Leeuwen, W.J.D.A., 1997. A comparison of vegetation indices over a global set of TM images for EOS-MODIS. *Remote Sens. Environ.* 59 (3), 440–451.
- Hulley, G.C., Göttsche, F.M., Rivera, G., Hook, S.J., Freepartner, R.J., Martin, M.A., Cawse-Nicholson, K., Johnson, W.R., 2022. Validation and quality assessment of the ECOSTRESS level-2 land surface temperature and emissivity product. *IEEE Trans. Geosci. Remote Sens.* 60, 1–23. <https://doi.org/10.1109/TGRS.2021.3079879>.
- Irmak, S., Allen, R.G., Whitty, E.B., 2003. Daily grass and alfalfa-reference evapotranspiration estimates and alfalfa-to-grass evapotranspiration ratios in Florida. *J. Irrig. Drain. Eng.* 129 (5), 360–370.
- Irons, J.R., Dwyer, J.L., Barsi, J.A., 2012. The next landsat satellite: the landsat data continuity mission. *Remote Sens. Environ.* 122, 11–21. <https://doi.org/10.1016/j.rse.2011.08.026>.
- Ivanov, V.Y., Vivoni, E.R., Bras, R.L., Entekhabi, D., 2004. Catchment hydrologic response with a fully distributed triangulated irregular network model. *Water Resour. Res.* 40 (11). <https://doi.org/10.1029/2004WR003218>.
- Jacquemoud, S., Verhoef, W., Baret, F., Bacour, C., Zarco-Tejada, P.J., Asner, G.P., François, C., Ustin, S.L., 2009. PROSPECT+SAIL models: a review of use for vegetation characterization. *Remote Sens. Environ.* 113, S56–S66.
- Joiner, J., Yoshida, Y., Zhang, Y., Duveiller, G., Jung, M., Lyapustin, A., Wang, Y., Tucker, C.J., 2018. Estimation of terrestrial global gross primary production (GPP) with satellite data-driven models and eddy covariance flux data. *Remote Sens. (Basel)* 10 (9), 1346.
- Joshi, C., Mohanty, B.P., Jacobs, J.M., Ines, A.V.M., 2011. Spatiotemporal analyses of soil moisture from point to footprint scale in two different hydroclimatic regions. *Water Resour. Res.* 47 (1). <https://doi.org/10.1029/2009WR009002>.
- Kljun, N., Calanca, P., Rotach, M.W., Schmid, H.P., 2015. A simple two-dimensional parameterisation for Flux Footprint Prediction (FFP). *Geosci. Model. Dev.* 8 (11), 3695–3713.
- Kogan, F., Salazar, L., Roytman, L., 2012. Forecasting crop production using satellite-based vegetation health indices in Kansas, USA. *Int. J. Remote Sens.* 33 (9), 2798–2814. <https://doi.org/10.1080/10413116.2011.621464>.
- Kool, D., Agam, N., Lazarovitch, N., Heitman, J.L., Sauer, T.J., Ben-Gal, A., 2014. A review of approaches for evapotranspiration partitioning. *Agric. For. Meteorol.* 184, 56–70.
- Lambers, H., Chapin III, F.S., Pons, T.L., 2008. *Plant Physiological Ecology*. Springer Science & Business Media.
- Li, J., Roy, D.P., 2017. A global analysis of sentinel-2A, sentinel-2B and landsat-8 data revisit intervals and implications for terrestrial monitoring. *Remote Sens. (Basel)* 9 (9). <https://doi.org/10.3390/rs9090902>. Article 9.
- Li, J., Song, J., Li, M., Shang, S., Mao, X., Yang, J., Adedoye, A.J., 2018. Optimization of irrigation scheduling for spring wheat based on simulation-optimization model under uncertainty. *Agric. Water Manage.* 208, 245–260. <https://doi.org/10.1016/j.agwat.2018.06.029>.
- Liang, L., Feng, Y., Wu, J., He, X., Liang, S., Jiang, X., de Oliveira, G., Qiu, J., Zeng, Z., 2022. Evaluation of ECOSTRESS evapotranspiration estimates over heterogeneous landscapes in the continental US. *J. Hydrol. (Amst)* 613, 128470.
- Liliane, T.N., Charles, M.S., 2020. Factors affecting yield of crops. *Agronomy-Climate Change Food Secur.* 9.
- Lin, S., Li, J., Liu, Q., Li, L., Zhao, J., Yu, W., 2019. Evaluating the effectiveness of using vegetation indices based on red-edge reflectance from sentinel-2 to estimate gross primary productivity. *Remote Sens. (Basel)* 11 (11). <https://doi.org/10.3390/rs11111303>. Article 11.
- Liu, L., Xiao, X., Qin, Y., Wang, J., Xu, X., Hu, Y., Qiao, Z., 2020. Mapping cropping intensity in China using time series Landsat and Sentinel-2 images and Google Earth Engine. *Remote Sens. Environ.* 239, 111624. <https://doi.org/10.1016/j.rse.2019.111624>.
- Liu, N., Oishi, A.C., Miniati, C.F., Bolstad, P., 2021. An evaluation of ECOSTRESS products of a temperate montane humid forest in a complex terrain environment. *Remote Sens. Environ.* 265, 112662. <https://doi.org/10.1016/j.rse.2021.112662>.
- Logan, K.E., Brunsell, N.A., 2015. Influence of drought on growing season carbon and water cycling with changing land cover. *Agric. For. Meteorol.* 213, 217–225. <https://doi.org/10.1016/j.agrformet.2015.07.002>.
- Ma, J., Xiao, X., Zhang, Y., Doughty, R., Chen, B., Zhao, B., 2018. Spatial-temporal consistency between gross primary productivity and solar-induced chlorophyll fluorescence of vegetation in China during 2007–2014. *Sci. Total Environ.* 639, 1241–1253.
- Ma, J., Yan, X., Dong, W., Chou, J., 2015. Gross primary production of global forest ecosystems has been overestimated. *Sci. Rep.* 5 (1), 1–9.
- Mahfouf, J.-F., Ciret, C., Ducharme, A., Irannejad, P., Noilhan, J., Shao, Y., Thornton, P., Xue, Y., Yang, Z.-L., 1996. Analysis of transpiration results from the RICE and PILPS workshop. *Glob Planet Change* 13 (1–4), 73–88.
- Mäkelä, A., Pulkkinen, M., Kolari, P., Lagergren, F., Berbigier, P., Lindroth, A., Loustau, D., Nikinmaa, E., Vesala, T., Hari, P., 2008. Developing an empirical model of stand GPP with the LUE approach: analysis of eddy covariance data at five contrasting conifer sites in Europe. *Glob. Chang. Biol.* 14 (1), 92–108.
- Markham, B., Barsi, J., Kvaran, G., Ong, L., Kaita, E., Biggar, S., Czaplak-Myers, J., Mishra, N., Helder, D., 2014. Landsat-8 operational land imager radiometric

- calibration and stability. *Remote Sens. (Basel)* 6 (12), 12275–12308. <https://doi.org/10.3390/rs61212275>. Scopus.
- Matsui, T., Lakshmi, V., Small, E.E., 2005. The effects of satellite-derived vegetation cover variability on simulated land-atmosphere interactions in the NAMS. *J. Clim.* 18 (1), 21–40.
- McPherson, R.A., Fiebrich, C.A., Crawford, K.C., Kilby, J.R., Grimsley, D.L., Martinez, J. E., Basara, J.B., Illston, B.G., Morris, D.A., Kloesel, K.A., 2007. Statewide monitoring of the mesoscale environment: a technical update on the Oklahoma Mesonet. *J. Atmos. Oceanic Technol.* 24 (3), 301–321.
- Meerdink, S.K., Hook, S.J., Roberts, D.A., Abbott, E.A., 2019. The ECOSTRESS spectral library version 1.0. *Remote Sens. Environ.* 230, 111196.
- Meng, J., Du, X., Wu, B., 2013. Generation of high spatial and temporal resolution NDVI and its application in crop biomass estimation. *Int. J. Digital Earth* 6 (3), 203–218. <https://doi.org/10.1080/17538947.2011.623189>.
- Miao, Q., Rosa, R.D., Shi, H., Paredes, P., Zhu, L., Dai, J., Gonçalves, J.M., Pereira, L.S., 2016. Modeling water use, transpiration and soil evaporation of spring wheat–maize and spring wheat–sunflower relay intercropping using the dual crop coefficient approach. *Agric. Water Manage.* 165, 211–229.
- Misra, G., Cawkwell, F., Wingler, M., 2020. Status of phenological research using sentinel-2 data: a review. *Remote Sens. (Basel)* 12 (17). <https://doi.org/10.3390/rs12172760>. Article 17.
- Monteith, J.L., 1965. Evaporation and environment. *Symp. Soc. Exp. Biol.* 19, 205–234.
- Morison, J.L., Gifford, R.M., 1984. Plant growth and water use with limited water supply in high CO₂ concentrations. I. Leaf area, water use and transpiration. *Funct. Plant Biol.* 11 (5), 361–374.
- Mu, Q., Zhao, M., Running, S.W., 2011. Improvements to a MODIS global terrestrial evapotranspiration algorithm. *Remote Sens. Environ.* 115 (8), 1781–1800.
- O’Keefe, K., Bell, D.M., McCulloh, K.A., Nippert, J.B., 2020. Bridging the Flux Gap: sap flow measurements reveal species-specific patterns of water use in a tallgrass prairie. *J. Geophys. Res.: Biogeosci.* 125 (2), e2019JG005446 <https://doi.org/10.1029/2019JG005446>.
- Ozdogan, M., Woodcock, C.E., 2006. Resolution dependent errors in remote sensing of cultivated areas. *Remote Sens. Environ.* 103 (2), 203–217. <https://doi.org/10.1016/j.rse.2006.04.004>.
- Paul-Limoges, E., Revill, A., Maier, R., Buchmann, N., Damm, A., 2022. Insights for the partitioning of ecosystem evaporation and transpiration in short-statured croplands. *J. Geophys. Res.: Biogeosci.* 127 (7), e2021JG006760.
- Peña-Barragán, J.M., Ngugi, M.K., Plant, R.E., Six, J., 2011. Object-based crop identification using multiple vegetation indices, textural features and crop phenology. *Remote Sens. Environ.* 115 (6), 1301–1316. <https://doi.org/10.1016/j.rse.2011.01.009>.
- Penman, H.L., 1948. Natural evaporation from open water, bare soil and grass. *Proc. R. Soc. London. Series A. Math. Phys. Sci.* 193 (1032), 120–145.
- Puig-Sirera, A., Rallo, G., Paredes, P., Paço, T.A., Minacapilli, M., Provenzano, G., Pereira, L.S., 2021. Transpiration and water use of an irrigated traditional olive grove with sap-flow observations and the FAO56 dual crop coefficient approach. *Water (Basel)* 13 (18). <https://doi.org/10.3390/w13182466>. Article 18.
- Raich, J.W., Rastetter, E.B., Melillo, J.M., Kicklighter, D.W., Steudler, P.A., Peterson, B. J., Grace, A.L., Moore III, B., Vorosmarty, C.J., 1991. Potential net primary productivity in South America: application of a global model. *Ecol. Appl.* 1 (4), 399–429. <https://doi.org/10.2307/1941899>.
- Ran, Y., Li, X., Sun, R., Kljun, N., Zhang, L., Wang, X., Zhu, G., 2016. Spatial representativeness and uncertainty of eddy covariance carbon flux measurements for upscaling net ecosystem productivity to the grid scale. *Agric. For. Meteorol.* 230, 114–127.
- Redmon, L.A., Horn, G.W., Krenzer Jr., E.G., Bernardo, D.J., 1995. A review of livestock grazing and wheat grain yield: boom or bust? *Agron. J.* 87 (2), 137–147. <https://doi.org/10.2134/agronj1995.00021962008700020001x>.
- Reichstein, M., Falge, E., Baldocchi, D., Papale, D., Aubinet, M., Berbigier, P., Bernhofer, C., Buchmann, N., Gilmanov, T., Granier, A., 2005. On the separation of net ecosystem exchange into assimilation and ecosystem respiration: review and improved algorithm. *Glob. Chang. Biol.* 11 (9), 1424–1439.
- Reichstein, M., Tenhunen, J.D., Rouspard, O., Ourcival, J.-M., Rambal, S., Dore, S., Valentini, R., 2002. Ecosystem respiration in two Mediterranean evergreen Holm Oak forests: drought effects and decomposition dynamics. *Funct. Ecol.* 16 (1), 27–39.
- Richardson, A.D., Anderson, R.S., Arain, M.A., Barr, A.G., Bohrer, G., Chen, G., Chen, J. M., Ciais, P., Davis, K.J., Desai, A.R., 2012. Terrestrial biosphere models need better representation of vegetation phenology: results from the North American Carbon Program Site Synthesis. *Glob. Chang. Biol.* 18 (2), 566–584.
- Running, S., Mu, Q., Zhao, M., 2015. MOD17A2H MODIS/terra Gross Primary Productivity 8-day L4 Global 500m SIN Grid V006. NASA EOSDIS Land Processes DAAC.
- Running, S.W., Nemani, R.R., Heinsch, F.A., Zhao, M., Reeves, M., Hashimoto, H., 2004. A continuous satellite-derived measure of global terrestrial primary production. *Bioscience* 54 (6), 547–560.
- Segovia-Cardozo, D.A., Franco, L., Provenzano, G., 2022. Detecting crop water requirement indicators in irrigated agroecosystems from soil water content profiles: an application for a citrus orchard. *Sci. Total Environ.* 806, 150492 <https://doi.org/10.1016/j.scitotenv.2021.150492>.
- Shi, S., Nan, L., Smith, K.F., 2017. The current status, problems, and prospects of alfalfa (*Medicago sativa* L.) breeding in China. *Agronomy* 7 (1), 1.
- Skakun, S., Vermote, E., Roger, J.-C., Franch, B., 2017. Combined use of Landsat-8 and Sentinel-2A images for winter crop mapping and winter wheat yield assessment at regional scale. *AIMS Geosci.* 3 (2), 163–186. <https://doi.org/10.3934/geosci.2017.2.163>.
- Souza, V.de A., Roberti, D.R., Ruhoff, A.L., Zimmer, T., Adamatti, D.S., Gonçalves, L.G.G. de, Diaz, M.B., Alves, R.de C.M., Moraes, O.L.de, 2019. Evaluation of MOD16 algorithm over irrigated rice paddy using flux tower measurements in Southern Brazil. *Water (Basel)* 11 (9), 1911.
- Storey, J., Roy, D.P., Masek, J., Gascon, F., Dwyer, J., Choate, M., 2016. A note on the temporary misregistration of Landsat-8 Operational Land Imager (OLI) and Sentinel-2 Multi Spectral Instrument (MSI) imagery. *Remote Sens. Environ.* 186, 121–122.
- Suyker, A.E., Verma, S.B., 2010. Coupling of carbon dioxide and water vapor exchanges of irrigated and rainfed maize–soybean cropping systems and water productivity. *Agric. For. Meteorol.* 150 (4), 553–563.
- Taiz, L., Zeiger, E., Moller, I.M., Murphy, A., 2015. Plant physiology and development. *Plant Physiol. Develop. Ed.* 6 <https://www.cabdirect.org/cabdirect/abstract/20173165866>.
- Thimijan, R.W., Heins, R.D., 1983. Photometric, radiometric, and quantum light units of measure: a review of procedures for interconversion. *HortScience* 18 (6), 818–822.
- Tilman, D., Balzer, C., Hill, J., Befort, B.L., 2011. Global food demand and the sustainable intensification of agriculture. *Proc. Natl Acad. Sci.* 108 (50), 20260–20264. <https://doi.org/10.1073/pnas.1116437108>.
- Tucker, B.B., Cox, M.B., Eck, H.V., 1971. Effect of rotations, tillage methods, and N fertilization on winter wheat production. *Agron. J.* 63 (5), 699–702. <https://doi.org/10.2134/agronj1971.00021962006300050012x>.
- Vadez, V., Kholova, J., Medina, S., Kakkera, A., Anderberg, H., 2014. Transpiration efficiency: new insights into an old story. *J. Exp. Bot.* 65 (21), 6141–6153.
- Velupuri, N.M., Senay, G.B., Singh, R.K., Bohms, S., Verdin, J.P., 2013. A comprehensive evaluation of two MODIS evapotranspiration products over the conterminous United States: using point and gridded FLUXNET and water balance ET. *Remote Sens. Environ.* 139, 35–49.
- Vermote, P.E.F., Roger, J.C., & Ray, J.P. (2015). *MODIS land surface reflectance science computing facility principal investigator: dr. Eric F. Vermote Web site: http://modis-sr. ltdri.org* Correspondence e-mail address: Mod09@ltdri.org. 35.
- Vivoni, E.R., Gutiérrez-Jurado, H.A., Aragón, C.A., Méndez-Barroso, L.A., Rinehart, A.J., Wyckoff, R.L., Rodríguez, J.C., Watts, C.J., Bolten, J.D., Lakshmi, V., 2007. Variation of hydrometeorological conditions along a topographic transect in northwestern Mexico during the North American monsoon. *J. Clim.* 20 (9), 1792–1809.
- Wagle, P., Gowda, P.H., Neel, J.P.S., Northup, B.K., Zhou, Y., 2020a. Integrating eddy fluxes and remote sensing products in a rotational grazing native tallgrass prairie pasture. *Sci. Total Environ.* 712, 136407 <https://doi.org/10.1016/j.scitotenv.2019.136407>.
- Wagle, P., Gowda, P.H., Northup, B.K., 2019a. Annual dynamics of carbon dioxide fluxes over a rainfed alfalfa field in the U.S. Southern Great Plains. *Agric. For. Meteorol.* 265, 208–217. <https://doi.org/10.1016/j.agrformet.2018.11.022>.
- Wagle, P., Gowda, P.H., Northup, B.K., 2019b. Dynamics of evapotranspiration over a non-irrigated alfalfa field in the Southern Great Plains of the United States. *Agric. Water Manage.* 223, 105727.
- Wagle, P., Gowda, P.H., Northup, B.K., Neel, J.P., Starks, P.J., Turner, K.E., Moriasi, D. N., Xiao, X., Steiner, J.L., 2021. Carbon dioxide and water vapor fluxes of multi-purpose winter wheat production systems in the US Southern Great Plains. *Agric. For. Meteorol.* 310, 108631.
- Wagle, P., Gowda, P.H., Northup, B.K., Starks, P.J., Neel, J.P.S., 2019. Response of tallgrass prairie to management in the U.S. southern great plains: site descriptions, management practices, and eddy covariance instrumentation for a long-term experiment. *Remote Sens. (Basel)* 11 (17). <https://doi.org/10.3390/rs11171988>. Article 17.
- Wagle, P., Gowda, P.H., Northup, B.K., Turner, K.E., Neel, J.P., Manjunatha, P., Zhou, Y., 2018. Variability in carbon dioxide fluxes among six winter wheat paddocks managed under different tillage and grazing practices. *Atmos. Environ.* 185, 100–108.
- Wagle, P., Skaggs, T.H., Gowda, P.H., Northup, B.K., Neel, J.P., 2020b. Flux variance similarity-based partitioning of evapotranspiration over a rainfed alfalfa field using high frequency eddy covariance data. *Agric. For. Meteorol.* 285, 107907.
- Wagle, P., Xiao, X., Gowda, P., Basara, J., Brunzell, N., Steiner, J., K.C. A., 2017. Analysis and estimation of tallgrass prairie evapotranspiration in the central United States. *Agric. For. Meteorol.* 232, 35–47. <https://doi.org/10.1016/j.agrformet.2016.08.005>.
- Wagle, P., Xiao, X., Scott, R.L., Kolb, T.E., Cook, D.R., Brunzell, N., Baldocchi, D.D., Basara, J., Matamala, R., Zhou, Y., 2015a. Biophysical controls on carbon and water vapor fluxes across a grassland climatic gradient in the United States. *Agric. For. Meteorol.* 214, 293–305.
- Wagle, P., Xiao, X., Suyker, A.E., 2015b. Estimation and analysis of gross primary production of soybean under various management practices and drought conditions. *ISPRS J. Photogramm. Remote Sens.* 99, 70–83.
- Wagle, P., Xiao, X., Torn, M.S., Cook, D.R., Matamala, R., Fischer, M.L., Jin, C., Dong, J., Biradar, C., 2014. Sensitivity of vegetation indices and gross primary production of tallgrass prairie to severe drought. *Remote Sens. Environ.* 152, 1–14.
- Wang, H., Li, X., Tan, J., 2020. Interannual variations of evapotranspiration and water use efficiency over an oasis cropland in arid regions of North-Western China. *Water (Basel)* 12 (5), 1239.
- Wang, L., Zhu, H., Lin, A., Zou, L., Qin, W., Du, Q., 2017. Evaluation of the latest MODIS GPP products across multiple biomes using global eddy covariance flux data. *Remote Sens. (Basel)* 9 (5), 418.
- Wang, Y.-P., Leuning, R., 1998. A two-leaf model for canopy conductance, photosynthesis and partitioning of available energy I: model description and comparison with a multi-layered model. *Agric. For. Meteorol.* 91 (1–2), 89–111.
- Wardlow, B.D., Egbert, S.L., Kastens, J.H., 2007. Analysis of time-series MODIS 250m vegetation index data for crop classification in the U.S. Central Great Plains. *Remote Sens. Environ.* 108 (3), 290–310. <https://doi.org/10.1016/j.rse.2006.11.021>.

- Wolanin, A., Camps-Valls, G., Gómez-Chova, L., Mateo-García, G., van der Tol, C., Zhang, Y., Guanter, L., 2019. Estimating crop primary productivity with Sentinel-2 and Landsat 8 using machine learning methods trained with radiative transfer simulations. *Remote Sens. Environ.* 225, 441–457. <https://doi.org/10.1016/j.rse.2019.03.002>.
- Wu, C., Munger, J.W., Niu, Z., Kuang, D., 2010. Comparison of multiple models for estimating gross primary production using MODIS and eddy covariance data in Harvard Forest. *Remote Sens. Environ.* 114 (12), 2925–2939.
- Wu, Y., Huang, M., Warrington, D.N., 2011. Growth and transpiration of maize and winter wheat in response to water deficits in pots and plots. *Environ. Exp. Bot.* 71 (1), 65–71. <https://doi.org/10.1016/j.envexpbot.2010.10.015>.
- Xiao, X., Biradar, C.M., Czarnecki, C., Alabi, T., Keller, M., 2009. A simple algorithm for large-scale mapping of evergreen forests in tropical America, Africa and Asia. *Remote Sens. (Basel)* 1 (3), 355–374.
- Xiao, X., Boles, S., Liu, J., Zhuang, D., Frolking, S., Li, C., Salas, W., Moore III, B., 2005a. Mapping paddy rice agriculture in southern China using multi-temporal MODIS images. *Remote Sens. Environ.* 95 (4), 480–492.
- Xiao, X., Hollinger, D., Aber, J., Goltz, M., Davidson, E.A., Zhang, Q., Moore III, B., 2004. Satellite-based modeling of gross primary production in an evergreen needleleaf forest. *Remote Sens. Environ.* 89 (4), 519–534.
- Xiao, X., Zhang, Q., Saleska, S., Hutrya, L., De Camargo, P., Wofsy, S., Frolking, S., Boles, S., Keller, M., Moore, B., 2005b. Satellite-based modeling of gross primary production in a seasonally moist tropical evergreen forest. *Remote Sens. Environ.* 94 (1), 105–122. <https://doi.org/10.1016/j.rse.2004.08.015>.
- Xin, F., Xiao, X., Cabral, O.M., White, P.M., Guo, H., Ma, J., Li, B., Zhao, B., 2020. Understanding the land surface phenology and gross primary production of sugarcane plantations by eddy flux measurements, MODIS images, and data-driven models. *Remote Sens. (Basel)* 12 (14), 2186.
- Xu, L., Myneni, R.B., Chapin III, F.S., Callaghan, T.V., Pinzon, J.E., Tucker, C.J., Zhu, Z., Bi, J., Ciais, P., Tømmervik, H., 2013. Temperature and vegetation seasonality diminishment over northern lands. *Nat. Clim. Chang.* 3 (6), 581–586.
- Yang, G., Pu, R., Zhao, C., Xue, X., 2014. Estimating high spatiotemporal resolution evapotranspiration over a winter wheat field using an IKONOS image based complementary relationship and Lysimeter observations. *Agric. Water Manage.* 133, 34–43. <https://doi.org/10.1016/j.agwat.2013.10.018>.
- Yu, W., Li, J., Liu, Q., Zeng, Y., Zhao, J., Xu, B., Yin, G., 2018. Global land cover heterogeneity characteristics at moderate resolution for mixed pixel modeling and inversion. *Remote Sens. (Basel)* 10 (6), 856.
- Yuan, W., Liu, S., Zhou, G., Zhou, G., Tieszen, L.L., Baldocchi, D., Bernhofer, C., Gholz, H., Goldstein, A.H., Goulden, M.L., Hollinger, D.Y., Hu, Y., Law, B.E., Stoy, P. C., Vesala, T., Wofsy, S.C., 2007. Deriving a light use efficiency model from eddy covariance flux data for predicting daily gross primary production across biomes. *Agric. For. Meteorol.* 143 (3), 189–207. <https://doi.org/10.1016/j.agrformet.2006.12.001>.
- Zhang, H.K., Roy, D.P., Yan, L., Li, Z., Huang, H., Vermote, E., Skakun, S., Roger, J.-C., 2018. Characterization of Sentinel-2A and Landsat-8 top of atmosphere, surface, and nadir BRDF adjusted reflectance and NDVI differences. *Remote Sens. Environ.* 215, 482–494. <https://doi.org/10.1016/j.rse.2018.04.031>.
- Zhang, K., Kimball, J.S., Running, S.W., 2016. A review of remote sensing based actual evapotranspiration estimation. In: *Wiley Interdisciplinary Reviews: Water*, 3, pp. 834–853.
- Zhang, X., Xiao, X., Qiu, S., Xu, X., Wang, X., Chang, Q., Wu, J., Li, B., 2022. Quantifying latitudinal variation in land surface phenology of *Spartina alterniflora* saltmarshes across coastal wetlands in China by Landsat 7/8 and Sentinel-2 images. *Remote Sens. Environ.* 269, 112810 <https://doi.org/10.1016/j.rse.2021.112810>.
- Zhang, Y., Xiao, X., Wu, X., Zhou, S., Zhang, G., Qin, Y., Dong, J., 2017. A global moderate resolution dataset of gross primary production of vegetation for 2000–2016. *Sci. Data* 4, 170165.
- Zheng, Y., Zhang, L., Xiao, J., Yuan, W., Yan, M., Li, T., Zhang, Z., 2018. Sources of uncertainty in gross primary productivity simulated by light use efficiency models: model structure, parameters, input data, and spatial resolution. *Agric. For. Meteorol.* 263, 242–257.
- Zhu, M., Liu, S., Xia, Z., Wang, G., Hu, Y., Liu, Z., 2020. Crop growth stage GPP-driven spectral model for evaluation of cultivated land quality using GA-BPNN. *Agriculture* 10 (8). <https://doi.org/10.3390/agriculture10080318>. Article 8.
- Zurita-Milla, R., Kaiser, G., Clevers, J., Schneider, W., Schaepman, M.E., 2009. Downscaling time series of MERIS full resolution data to monitor vegetation seasonal dynamics. *Remote Sens. Environ.* 113 (9), 1874–1885.